Icarus 429 (2025) 116417

Contents lists available at ScienceDirect

Icarus

journal homepage: www.elsevier.com/locate/icarus

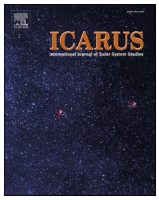

Night O_2 ($a^1\Delta_g$) airglow spatial distribution and temporal behavior on Venus based on SPICAV IR/VEx nadir dataset

D. Evdokimova [a,*], A. Fedorova [a], M. Zharikova [b,a], F. Montmessin [c], O. Korablev [a], L. Soret [d], D. Gorinov [a], D. Belyaev [a], J.-L. Bertaux [e]

[a] Space Research Institute of the Russian Academy of Sciences, Moscow, Russia
[b] HSE University, Moscow, Russia
[c] LATMOS, CNRS, UVSQ, Guyancourt, France
[d] LPAP, STAR Institute, Université de Liège, Liège, Belgium
[e] LATMOS, CNRS, Sorbonne Université, Paris, France

ARTICLE INFO

Dataset link: Night O2 (a1Δg) airglow based on SPICAV IR/VEx nadir dataset (Original data)

Keywords:
Venus
Atmosphere
IR spectroscopy

ABSTRACT

The infrared O_2 ($a^1\Delta_g$) airglow driven by the subsolar to antisolar circulation occurs between two global circulation regimes on Venus: the zonal super-rotation below 90 km and the subsolar to antisolar circulation over 120 km. Here we report the complete global results of SPICAV IR/Venus Express observations of O_2 ($a^1\Delta_g$) nightglow from 2006 till the end of the mission in 2014. The spectrometer resolving power of ~1000 at the considered spectral range was the highest among Venus Express instruments, and it was sufficient to resolve O_2 ($a^1\Delta_g$) airglow and thermal emission signals. The nadir spectra were fitted to a model representing these two phenomena ensuring robust separation of the thermal emission, and so retrieval of the airglow intensity. Its spatial distribution in the night hemisphere, averaged among 8 years of observations, shows the maximum intensity of 1.4 ± 0.8 MR located at 23H30 of local time and 0–5° N of latitude. A high variability of the airglow was observed. "Bright spots", i.e., those with an intensity above the global maximum, were observed over a latitude range of 70°S-70°N with the majority occurring around the antisolar point. Lack of imaging capability was an obstacle to track the short-term variations by SPICAV IR. A single observation sequence of 20 days covering neighboring locations exhibits indications of airglow intensity fluctuations with a 5.4-day periodicity. SPICAV IR working period covered the end of the 23rd Solar cycle and the solar activity increase of the 24th Solar cycle. A correlation of the O_2 ($a^1\Delta_g$) with the EUV solar flux increase predicted by global circulation model simulations was not found.

1. Introduction

The detection of ground-state oxygen on Venus remains an open question, its upper limit being set at about 0.3 ppm (Mills, 1999). However, photolysis of CO_2 and other species in the sunlit atmosphere sustains a high flux of oxygen atoms forming O_2 molecules in three-body recombination occurring at a high rate of ~10^{13} cm^{-2} s^{-1} (Krasnopolsky, 2006). One chain of this process leads to the formation of metastable O_2 ($a^1\Delta_g$) molecules. It is followed by a radiative relaxation, accompanied by the 1.27 μm emission, which constitutes the brightest oxygen airglow observed on Venus (Bougher et al., 1997).

$$2O + CO_2 \rightarrow O_2^* \left(a^1\Delta_g\right) + CO_2$$

$$O_2^* \left(a^1\Delta_g\right) \rightarrow O_2 \left(X^3\Sigma_{g^-}\right) + h\nu$$

The first identification of the 1.27-μm infrared emission on Venus was made in 1975 from ground-based observations (Connes et al., 1979), with an intensity of ~1 MR (1 MR = 10^{16} photons/m^2/s into 4π sr). Since then, the O_2 ($a^1\Delta_g$) airglow was repeatedly observed by various experiments at night, namely the O_2 ($a^1\Delta_g$) "nightglow" (Alien et al., 1992; Bougher and Borucki, 1994; Crisp et al., 1996). Images of the Venus night side showed discrete spots observed mainly near the antisolar point (Alien et al., 1992; Crisp et al., 1996; Lellouch et al., 1997; Ohtsuki et al., 2005; Gérard et al., 2008; Ohtsuki et al., 2008a; Bailey et al., 2008a; Piccioni et al., 2009; Shakun et al., 2010; Soret et al., 2012). This pattern is largely determined by circulation in the

* Corresponding author.
E-mail address: daria.evdokimova@cosmos.ru (D. Evdokimova).

https://doi.org/10.1016/j.icarus.2024.116417
Received 29 March 2024; Received in revised form 6 November 2024; Accepted 27 November 2024
Available online 3 December 2024

Venus lower thermosphere above 120 km. A strong temperature contrast between the sunlit and the dark parts of the atmosphere at these altitudes generates fluxes propagating from the subsolar (SS) to the antisolar (AS) point, and forming so-called subsolar-to-antisolar (SSAS) circulation (Bougher et al., 1997). This represents a constant supply of the Venus night hemisphere with photolysis products of CO_2 and other species, that include oxygen atoms. Around the AS point, the fluxes converge and plunge into deeper atmospheric layers. This mechanism is supported by the discovery of a warm layer around the AS point in a stellar occultation experiment (Bertaux et al., 2007a, 2007b; Piccialli et al., 2015). The temperatures at 90–100 km increase from 180 K to 230 K with the solar-zenith angle (SZA) in the night hemisphere, and it is likely related to the air adiabatic heating by the downward flow (Bertaux et al., 2007b). The rotational temperatures of O_2 ($a^1\Delta_g$) airglow forming in the same altitude range is a proxy for mesosphere temperatures. Spatially resolved ground-based observations from different facilities found average O_2 ($a^1\Delta_g$) rotational temperatures 183–189 K (Ohtsuki et al., 2008b) and 181–196 K (Bailey et al., 2008a; Bailey et al., 2008b).

The altitude of the emission was theoretically predicted at 90–115 km (Alien et al., 1992; Crisp et al., 1996; Bougher et al., 1997). It was for the first time confirmed directly using limb observations by the VIRTIS imaging spectrometer on board the Venus Express (VEx) spacecraft of the European Space Agency (ESA) (Drossart et al., 2007b). Instead of being quenched by collisions with CO_2, about 80 % of the excited O_2 ($a^1\Delta_g$) molecules emit photons at altitudes where the airglow reaches its maximum intensity (Gérard et al., 2008). In general, the altitude of the O_2 ($a^1\Delta_g$) airglow intensity maximum tended to increase towards the terminator (Soret et al., 2012; Gérard et al., 2014) varying within 90–103 km with an average value of 96 ± 2 km (Gérard et al., 2010).

The nightglow altitude appears located in the transition region between two global circulation patterns of the Venus atmosphere: the zonal supper-rotation below 90 km and the SSAS circulation over 120 km. The transition between them is not yet fully characterized, and the O_2 ($a^1\Delta_g$) emission is an important circulation tracer for remote sensing of this altitude range. The radiative lifetime of O_2 ($a^1\Delta_g$) state is ~4300 s (Miller et al., 2001), and it is twice as long as the measured time of an airglow bright patch displacement (Hueso et al., 2008; Soret et al., 2014). Based on these results, it was suggested that the changing airglow morphology could represent winds at 96 km (Hueso et al., 2008; Soret et al., 2014; Gorinov et al., 2018; Shakun et al., 2023). Using the VIRTIS-M consecutive snapshots, velocity vectors were estimated in the range of 0–213 m/s with an average of 54 m/s at ~96 km (Soret et al., 2014). Independent analyses by Hueso et al. (2008), Gorinov et al. (2018) and Shakun et al. (2023) showed that the zonal flows of SSAS circulation converge at 22.5 ± 0.5 h of local time. However, the O_2 ($a^1\Delta_g$) bright spots are not only affected by horizontal transport. The intensity changes can also be caused by vertical transport (Alien et al., 1992; Crisp et al., 1996; Gérard et al., 2014; Soret et al., 2014; Navarro et al., 2021) and changes in chemical recombination of atomic oxygen or by variations in atmospheric temperature or density (Ohtsuki et al., 2008a; Navarro et al., 2021). According to the Venus Planetary Climate Model (Venus PCM) (Navarro et al., 2021), a change of volume emission rate at 95 km would be 50 % due to chemical contribution, 30 % due to horizontal transport, and 20 % due to vertical transport. O_2 ($a^1\Delta_g$) bright spots at latitudes above 30° with intensities exceeding 2 MR should be mainly influenced by supplying or removing of O atoms (Navarro et al., 2021). Chemical contribution results also in keeping the nightglow patches active longer than the lifetime of O_2 ($a^1\Delta_g$) state or, conversely, their dramatic variations on 1-day scale. Vertical transport by different types of gravity waves can explain some patterns of observed effects including double intensity peaks in the vertical profile (Altieri et al., 2014), short-term variability around the anti-solar point (Brecht et al., 2011; Hoshino et al., 2012), and the propagation of airglow spots to high latitudes (Navarro et al., 2021), but cannot reproduce the overall high level of nightglow variability. The most recent global circulation models showed substantial impact of upward propagation of Kelvin waves appearing in the middle cloud layer (Nara et al., 2020; Navarro et al., 2021; Takagi et al., 2022). It is proposed to be a cause of O_2 ($a^1\Delta_g$) bright spots transferring to high latitude, suggesting short-term variations (~4 days) of their brightness (Navarro et al., 2021). This periodicity was observed in the cloud tops (Nara et al., 2019, 2020) and in EUV dayglow (Masunaga et al., 2015, 2017). Retrieved wind flow disturbances possibly related to underlying mountains were identified in the airglow dataset despite the high altitude of the emission (Gorinov et al., 2018). The topography influence on wind has been derived for the cloud level altitudes (Bertaux et al., 2016; Khatuntsev et al., 2017; Fukuhara et al., 2017; Kouyama et al., 2017), and mountain waves have been shown theoretically to be capable of propagating above 90 km (Mingalev et al., 2015).

Venus Express worked at the end of the 23rd Solar cycle and the first half of the 24th Solar cycle. The UV solar flux periodicity is the main external force driving the changes in the thermosphere through the EUV heating on the day side above 130 km. Bougher and Borucki (1994) studied an influence of different solar flux conditions on the nightglow intensities in the framework of the VTGCM (Venus Thermospheric General Circulation Model). Maximum and minimum fluxes differed by a factor of 3 causing the nightglow peak intensity change by ~40 % (Bougher and Borucki, 1994). In 2006–2008, the EUV solar flux changed just by 10.4 % during the period covered by VIRTIS-M observations, and a correlation analysis has found no evidence of the link with the O_2 ($a^1\Delta_g$) airglow brightness variability (Soret and Gérard, 2015).

We present the first complete analysis of the O_2 ($a^1\Delta_g$) airglow observations carried out by the infrared (IR) channel of the SPICAV (SPectroscopy for the Investigation of the Characteristics of the Atmosphere of Venus) spectrometer over an unprecedented continuous period of 8 years. This work covers almost the whole night hemisphere, and extends the coverage of VIRTIS-M (2006–2008; Soret et al., 2014) by 6 more years. The SPICAV IR experiment is described in Section 2. The O_2 emission signal obtained by SPICAV IR is robustly extracted from measured data contaminated by the thermal emission of the planet using a radiative transfer model described in Section 3. VIRTIS-M and SPICAV IR were part of the Venus Express payload and performed a few joint observations dedicated to cross validation. Section 4 considers in detail retrieved O_2 ($a^1\Delta_g$) airglow data from collaborative observations. The nightglow statistical map accumulated for 8 years of observations, a detailed study of the brightest spots, short-term changes and a correlation analysis with the solar activity increase in 2008–2014 are presented in Section 5 with conclusions in Section 6.

2. SPICAV IR data description

SPICAV on Venus Express consisted of infrared (SPICAV IR) and ultraviolet (SPICAV UV) channels (Bertaux et al., 2007a). SPICAV IR was developed at the Space Research Institute of the Russian Academy of Sciences (IKI RAS), and its design was based on the IR channel of the SPICAM (SPectroscopy for the Investigation of the Characteristics of the Atmosphere of Mars) spectrometer working on board the Mars Express spacecraft (Korablev et al., 2006; Korablev et al., 2012). The principal feature of the spectrometer is an acousto-optic tunable filter (AOTF): a birefringent crystal of TeO_2 with attached piezoelectric transducers generating acoustic waves of radio frequency 80–250 MHz. The system takes advantage of the Bragg's diffraction of light on an ultrasonic acoustic wave, becoming a narrowband variable filter. One SPICAV IR spectrum is recorded sequentially by adjusting the AOTF filter to a series of required wavelengths. The filter produced two separate output beams with orthogonal polarization focused on two detectors. The instrument's main optical aperture allowed for the nadir and limb observations within a circular field of view (FOV) of 2° of diameter (Korablev et al., 2012). The Venus Express orbit was elongated with a pericenter close to the North Pole, and the spacecraft altitude varied from 250 km to 66,000 km. As a consequence, the footprint diameter changed within a

range of 9–2300 km in nadir, and the observations of the Southern Hemisphere had lower spatial resolution.

The full spectral range of SPICAV IR is 0.65–1.7 μm. Two Si-InGaAs photodiode detectors collect the two beams' signal. The silicon layer is sensitive to the short-wavelength radiation within 0.65–1.05 μm spectral range, while the interval of 1.05–1.7 μm is sensed by the InGaAs detector. To reduce the dark current, the detectors can be cooled by built-in Peltier elements. The current study focuses on the long-wavelength spectral interval, where the mean spectral resolution is 5.2 cm^{-1} or ~ 1 nm. The integration time of one spectral point was 44.8 or 89.6 ms for night-side observations. This results in an extended duration of the entire spectrum measurement. To obtain the maximum amount of information during an orbit, the full spectral range of SPICAV IR was restricted to 1.05–1.3 μm for the majority of observations of the Venus night side. To reduce the time required for a single spectrum measurement, it is also possible to increase the wavelength interval between consecutive spectral points. The maximal and minimal wavelength steps are about 2 and 7 nm, respectively. Examples of the measured spectra are provided in the Supplementary material (Fig. S1). The details of the instrument's calibrations can be found in Korablev et al. (2012). The measured signal was separated from the dark current recorded independently at the beginning and end of an integration period. The signal-to-noise ratio (SNR) has been estimated during the Venus Express cruise phase by observing the Sun and Venus. It is equal to 50 for the longest exposure time of 89.6 ms and enabled Peltier coolers, and the SNR is reduced by a factor of 2 without cooling the detectors (Korablev et al., 2012). Measurement uncertainties of the spectrum are estimated based on the SNR value proportionally to the square root of exposure time. The wavelength calibrations are done based on the AOTF parameters and the wavelength uncertainty is less than 0.2 nm (Fedorova et al., 2015).

The SPICAV IR instrument was working during the entire mission duration from April 2006 to December 2014. One of the main issues for infrared emission observations is contamination from the sunlit hemisphere. In the analysis, the SZA was limited in the range 95–180° to minimize the sunlight influence. The corresponding local time range was approximately from 18:20 to 5:40. This bulk of data was accumulated almost over the entire Venus' disk, where each year of observations was covering a different part of the globe. However, the instrument's footprint, variable along the orbit, made the coverage sparse in the Northern Hemisphere, while observations of the Southern Hemisphere were spatially smoothed. The calibrated data and the observational geometry information are publicly available in the ESA's Planetary Science Archive (PSA).

Large footprints located in the Southern Hemisphere close to the terminator include a fraction of scattered solar radiation seen as a continuous spectral background. This contribution was removed from the spectra by linear interpolation based on intervals 1.21–1.25 and 1.29–1.3 μm. In case of a strong contamination, the spectrum has been excluded from the analysis. We also exclude contaminated spectra that are measured in limited spectral ranges and that do not contain information suitable for the background elimination. The data set comprised more than 2300 sessions of observations, which correspond to approximately 20,000 spectra. Of these, approximately half were obtained in nadir. The spatial coverage and resolution of these observations are presented in Fig. 1. The annual coverage is presented in the Supplementary material, Fig. S2.

3. Data analysis

The extraction of the oxygen emission signal requires consideration of (1) a Venus thermal emission model and (2) a theoretical definition of O_2 ($a^1\Delta_g$) airglow. The thermal emission of the Venus lower atmosphere and surface escapes to outer space in the atmospheric transparency windows, i.e., a narrow spectral interval between strong CO_2 absorption bands (Crisp et al., 1991). Radiation in the 1.1- and 1.18-μm transparency windows originates from the 0–15 km altitude range. The 1.28-μm transparency window emission is formed at 15–30 km (Taylor et al., 1997). The 1.1- and 1.18-μm transparency windows are spectrally close to the O_2 ($a^1\Delta_g$) band that comprise lines within the 1.25–1.29 μm interval. The 1.28-μm transparency window overlaps the airglow spectrum. The spectral resolution of SPICAV IR is sufficient to robustly identify the nightglow over the 1.28-μm transparency window spectra. However, simultaneous modeling of O_2 ($a^1\Delta_g$) airglow and thermal emission spectra for correct evaluation of the nightglow intensity is necessary.

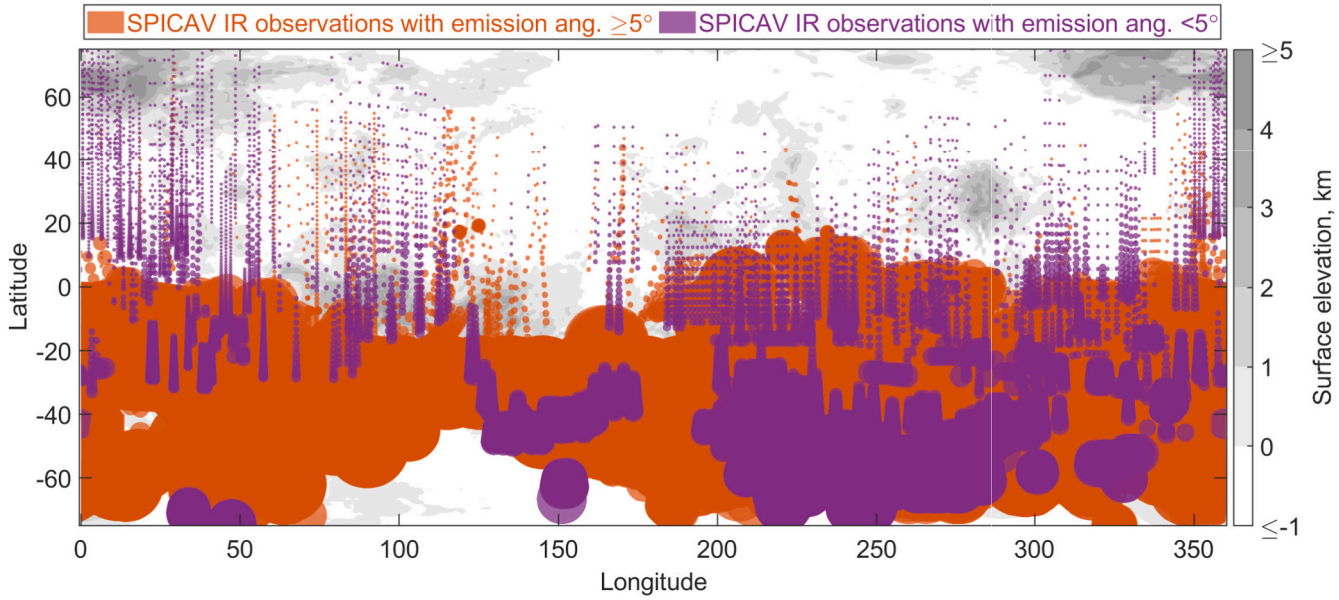

Fig. 1. Spatial distribution of individual measurements. Circles represent the footprint of SPICAV IR when its diameter exceeds 100 km. For visualization purposes, diameters of smaller areas are set to 100 km. The Magellan global topography data from the NASA Planetary Data System (Saunders et al., 1992) is displayed underneath. Violet circles show near-nadir observations with emission angles <5°. Red circles represent observations with emission angles 5–60° and footprints <3000 km in diameter. (For interpretation of the references to colour in this figure legend, the reader is referred to the web version of this article.)

3.1. Direct model of the nadir Venus thermal emission

Transparency windows spectra are reproduced by a 1-D radiative transfer model with multiple scattering. The SHDOMPP program is used to solve the radiative transfer equation using the method of discrete ordinates and spherical harmonics under approximation of a plane-parallel atmosphere (Evans, 2007). The routine was adapted to 1.1, 1.18 and 1.28-μm windows' spectra by Fedorova et al. (2015). Radiative transfer is calculated line by line with the spectral step of 0.1 cm^{-1}. A convolution with the AOTF function is carried out to simulate the spectral resolution of the SPICAV IR spectrometer (Korablev et al., 2012).

The input parameters of the model are the profiles of temperature, pressure, and CO_2 mixing ratio from the VIRA database (Seiff et al., 1985). Surface temperature is set to the atmospheric temperature at the lowest profile altitude. Radiative transfer is calculated on an altitude grid from the surface elevation level to 80 km with a step of 1 km. The spectral range covers the water vapor absorption at 1.1–1.18 μm, and the model simulates the absorption by CO_2 and H_2O. The CO_2 mixing ratio is equal to 0.965. The water vapor is assumed to be uniformly mixed below the clouds and its mixing ratio is a variable parameter. The CO_2 absorption is calculated according to the high-temperature spectroscopic database «High-T» tuned for these windows (Pollack et al., 1993; Tashkun et al., 2003; Bézard et al., 2011; Fedorova et al., 2015). The absorption of water vapor in the lower atmosphere is modeled based on the BT2 line list (Barber et al., 2006). The absorption line shapes are set in accordance to the previous studies (Bézard et al., 2011; Fedorova et al., 2015). Rayleigh scattering by carbon dioxide molecules is also taken into account. The gaseous, specifically CO_2, absorption in the IR is more complex to handle at the high temperature and pressure conditions of the Venusian atmosphere. The observations showed that it is necessary to consider the CO_2 continuum (Pollack et al., 1993), i.e., the superposition of very distant wings of strong permitted CO_2 bands and the possible collision-induced transitions with this molecule. It is generally parameterized with a coefficient α, expressed in $cm^{-1}amagat^{-2}$ (1 amagat = 2.6867774×10^{19} molecules cm^{-3}). Continuum coefficient possible values were limited to the 1.1-μm, 1.18-μm and 1.28-μm windows in the ranges of $(0.29–0.66) \times 10^{-9}$ $cm^{-1}amagat^{-2}$, $(0.30–0.78) \times 10^{-9}$ $cm^{-1}amagat^{-2}$ and $< 2 \times 10^{-9}$ $cm^{-1}amagat^{-2}$ respectively, as described in the work of Fedorova et al. (2015). For the defined ranges, the continuum level was empirically chosen equal to 0.75×10^{-9} $cm^{-1}amagat^{-2}$ and 0.38×10^{-9} $cm^{-1}amagat^{-2}$ for transparency windows of 1.28 and 1.1–1.18 μm respectively. By this definition, the CO_2 continuum does not influence the O_2 ($a^1\Delta_g$) airglow analysis.

The scattering parameters of the cloud layer are computed according to the Mie theory (Mishchenko et al., 2002). The chosen cloud model is an update in comparison with the previous study of Fedorova et al. (2015). It follows the work of Haus et al. (2016) that assumes spherical-shaped aerosol particles composed of 75 %-H_2SO_4 water solution. The density profiles of aerosols are computed according to the parameters that are set in Table 1 of Haus et al. (2016). The aerosol particle sizes of four modes are assumed to be distributed according to log-normal law. The modal radii are 0.3, 1.0, 1.4, 3.65 μm for modes 1, 2, 2′ and 3 respectively. Dispersion of modal sizes' distributions are 1.56, 1.29, 1.23, 1.28 (Pollack et al., 1993). Refractive index of H_2SO_4-acid solution was taken from Palmer and Williams (1975). To minimize the number of parameters, the particle densities of mode 2 and 3 are adjusting jointly to describe aerosol scattering. The total vertical density profiles of mode 2 and 3 are multiplied by a scaling parameter. In the narrow interval of the 1.28-μm transparency window spectral range, H_2SO_4 optical constants do not change. The window spectrum shape is not influenced by the particle density variations, and scattering in the clouds behaves as a "gray" background.

In general, the developed thermal emission model requires three free parameters: a scaling parameter adjusting mode 2 and 3 particle densities in the cloud layer, the water vapor volume mixing ratio in the lower atmosphere of Venus and the surface emissivity. The observation geometry defines the surface altitude for each transparency window and the emission angle.

3.2. Oxygen emission model

In the current study, we follow the approach developed to simulate the terrestrial O_2 ($a^1\Delta_g$) airglow spectrum (Sun et al., 2018; Bertaux et al., 2020). The computation of the spectrum is done line-by-line for the main isotope $^{16}O^{16}O$ using transitions from the HITRAN 2016 database. For each emission line, the emission rate per molecule (ϵ) is computed by multiplying the Einstein coefficient A_{21} for this transition (k) by the relative population of the excited energy level (Eq. 1). The relative population is the ratio between the partition sum of the excited energy level Q(J'(k), T) and the total partition sum $Q_{tot}^{up}(T)$ at the particular temperature T.

$$\epsilon(k) = A_{21}(k)\ \frac{Q(J'(k),T)}{Q_{tot}^{up}(T)} \tag{1}$$

The partition sum of J'(k) energy level is computed assuming that the number of excited molecules follows the Boltzmann distribution, thus, is determined by temperature T. The detailed algorithm and justification can be found in Bertaux et al. (2020).

The pressure broadening is ineffective in the upper mesosphere; the broadening of airglow lines depends on the temperature. However, the thermal broadening is several orders of magnitude smaller than the width of the SPICAV IR AOTF function, thus, the O_2 ($a^1\Delta_g$) airglow lines are not resolved.

We assume constant rotational temperature of the molecules to compute the emission spectrum. The SPICAV spectra are not sensitive to observed rotational temperature variations (Bailey et al., 2008b), due to the limitations of both the low SNR and the spectral resolution. The temperature is set to 195 K that is an average O_2* rotational temperature according to ground-based observations (Bailey et al., 2008b). The sum of the emission lines, multiplied by emitting molecule column density, composes the O_2 ($a^1\Delta_g$) airglow spectrum. Self-absorption of O_2 in the upper atmosphere is neglected because its abundance is small. The CO_2 absorption in the atmosphere column over the airglow layer is negligible as well (Crisp et al., 1996).

3.3. Inverse problem

Parameters that provided the minimum reduced χ^2-value (Eq. 2) of the experimental spectrum R_{exp} and the modeled one were considered as the solution. The modeled spectrum is the sum of the thermal radiance $R_{thermal}$ and O_2 ($a^1\Delta_g$) airglow R_{O2}. The computation of reduced χ^2-value considers the 1.05–1.3 μm spectral range. The surface height in the observing location is z_0, which determines the initial level for the radiative transfer computation. The measurement uncertainties σ_{exp} are estimated using the SNR ratio of the instrument (Korablev et al., 2012).

$$\chi^2(z_0, SF, VMR_{H2O}, EMIS, D_{O2}) = \frac{1}{N-5}\sum_{\lambda_1}^{\lambda_N}\left(\frac{R_{exp}(\lambda, z_0) - R_{thermal}(\lambda, z_0, SF, VMR_{H2O}, EMIS) - R_{O2}(\lambda, D_{O2})}{\sigma_{exp}(\lambda)}\right)^2 \tag{2}$$

The model set up to handle the experimental data is defined by four parameters:

(1) scaling parameter applied to distributions of mode 2 and 3 particles in the cloud layer (SF in Eq. 2),
(2) water vapor volume mixing ratio in the lower atmosphere of Venus (VMR_{H2O} in Eq. 2),
(3) surface emissivity for the 1.1-μm window (EMIS in Eq. 2),
(4) column density of O_2* molecules (D_{O2} in Eq. 2).

Synthetic Venus thermal spectra are fitted to the measurements using a look-up table. It represents the calculated radiation intensity for parameter values in the intervals: 70–240 % for the scaling factor of mode 2 and 3 particle density with a step of 5 %, 2–50 ppm for the H_2O VMR with a step of 2 ppm and 70–95 % for surface emissivity with a step of 5 %. Surface temperature is set accordingly with the topography, and the radiation was modeled for various initial heights. Their values are set in the range from −2 to 9 km with a step of 1 km. In some observations of the Northern Hemisphere, the SPICAV IR footprints for 1.18-μm and 1.28-μm windows are strongly displaced. It becomes necessary for these spectra to fit the 1.28-μm window spectrum separately.

Fig. 2 show an example of the data analysis for orbit #3020A02. In the range of 1.275–1.285, i.e., transparency window maximum, the model allows a correct extraction of thermal emission (Fig. 2B). Fig. 2C presents the retrieved and modeled O_2 ($a^1\Delta_g$) airglow spectra.

Airglow intensities are converted to the total emission brightness expressed in MR by spectrally integrating the O_2 emission radiance calibrated in W/m^2/μm/sr and correcting the airglow intensity according to emission angle (θ) and cloud backscattering. Emitted downward radiation backscattered at the cloud tops is considered through a correction coefficient a = 0.875 (Crisp et al., 1996).

$$I[MR] = \frac{1}{10^{10}hc}\int \frac{4\pi R\lambda}{(sec\theta + 2a)}d\lambda = \frac{503 \bullet 4\pi}{(sec\theta + 2 \bullet 0.875)}\int R\left[\frac{W}{m^2\mu m\, sr}\right]\lambda[\mu m]d\lambda[\mu m] \quad (3)$$

The extracted O_2 ($a^1\Delta_g$) airglow intensity is calculated from the radiance by Eq. 3 using the trapezoidal rule. In order to obtain the intensity, the integration limits should be set at 1.25 μm and 1.29 μm, as can be seen in Fig. 2C. However, the spectral interval for Eq. 3 was restricted to 1.2635–1.2750 μm to avoid adding noise to the integration. According to the model, this spectral range comprises 78 % of the O_2 ($a^1\Delta_g$) airglow intensity. Therefore, the result of the integration within 1.2635–1.2750 μm has to be divided by a factor of 0.78 to obtain the observed nightglow intensity.

Observations characterized by large footprints may be affected by spatial non-uniformity and atmospheric curvature. SPICAV IR measures an average of the airglow signal over the entire area. We assume the airglow to be uniform in this area. Then, a correction factor is evaluated by averaging the Eq. 3 for a set of emission angles defined by the observational geometry. For the emission angles lower than 60° and footprints smaller than 3000 km in diameter the maximum correction is below 10 %.

The uncertainty of the oxygen airglow brightness originates from the signal error and a model systematic uncertainty. The resulting SPICAV's absolute calibration was estimated to be within ±10 % interval for all pairs of exposure times and gain values (Korablev et al., 2012). The radiative transfer modeling and a typical observed oxygen airglow spectrum differ by a non-zero residual of ~0.01 W/m^2/μm/sr in the maximum and the right wing of the 1.28-μm transparency window visible in Fig. 2C. This mismatch is low, but still is twice as large as the signal noise, and it is spectrally narrow. It cannot be ascribed to variation of the oxygen rotational temperature in the model. The spectral width of the discrepancy means also no relation to aerosol optical properties. The emissivity and water vapor variations cannot yield a

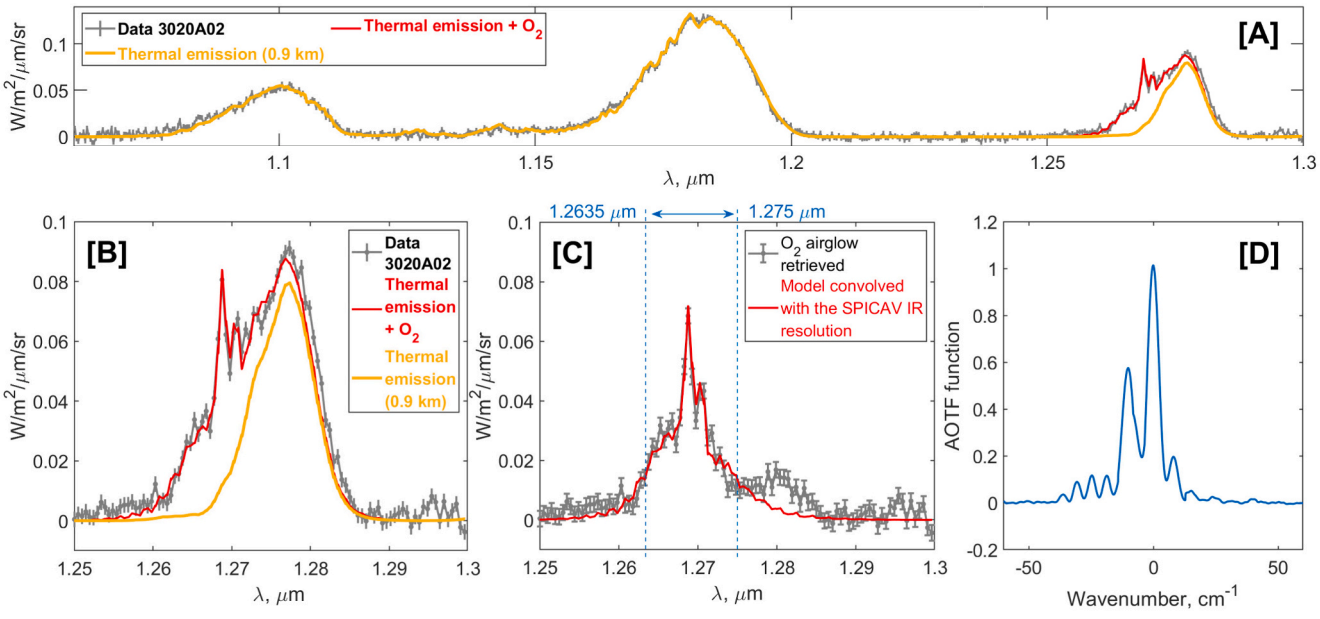

Fig. 2. Example of data analysis for one measurement of a nadir session during orbit #3020A02 (26 July 2014) (A) Gray curve with error bars shows the measured spectrum covering the three atmospheric transparency windows. The red curve is the best-fit model of thermal radiation and O_2 ($a^1\Delta_g$) airglow, while the yellow colour shows only thermal contribution. Model parameters are: SF = 141 ± 0.1 %, VMR_{H2O} = 25.2 ± 0.04 ppmv, EMIS = 0.85 ± 0.01. (B) Panel B is a zoom of the third atmospheric window encompassing the O_2 emission. (C) O_2 ($a^1\Delta_g$) emission band at 1.27 μm, which is the residual between the thermal model and the experiment, and the O_2 model is plotted in red (1.3 ± 0.1 MR). Airglow emission is integrated within 1.2635–1.2750 μm indicated by the blue dashed lines. The interval comprises 78 % of the O_2 airglow signal, and the derived intensities are corrected to account for it. (D) SPICAV IR instrument function, i.e., the AOTF bandpass function. (For interpretation of the references to colour in this figure legend, the reader is referred to the web version of this article.)

radiance change larger than 1 %. Here, we present two plausible explanations of the discrepancy. The first one is an uncertainty of the AOTF function, in particular, in its wings. In the beginning of the SPICAV IR scientific mission, a modification of the instrumental function was noted. The AOTF function has been revised in this spectral range based on the first SPICAV IR limb observations of O_2 ($a^1\Delta_g$) airglow in order to have absent thermal emission signal. Parametrization of two main maxima has been improved. Limb observations were done with similar exposure time as nadir measurements and had also rather high noise. It complicates accurate characterization of the AOTF function wings which are crucial to describe the convolved airglow spectrum at wavelengths longer than 1.275 μm. The second reason might be related to deficiencies of the used radiative transfer model linked to CO_2 absorption spectroscopy uncertainties, such as a CO_2 line shape, unknown line intensities at high temperatures and pressures or the CO_2 continuum. It is known that CO_2 line shape differs from the Voigt profile in the line wings, i.e., sub-Lorentzian line shape. In this work we assume an empirical correction for CO_2 line shape by Bézard et al. (2011) and the CO_2 continuum coefficient is constant within the 1.28-μm transparency window. So far, this spectral range is poorly studied by laboratory measurements. Further investigation of CO_2 spectroscopy is important for better description of the Venus transparency window spectra. Since the positive residual in 1.28–1.29 μm has not been corrected, the intensity of the bump is included in the retrieval uncertainties of O_2 brightness. It is the main uncertainty defining the detection limit of O_2 ($a^1\Delta_g$) airglow signal, estimated equal to 0.13 MR on average.

4. Comparison with VIRTIS-M observations

The spectral range of oxygen airglow has also been covered by the infrared channel of the VIRTIS-M imaging spectrometer, which spectral range was from 1 to 5.1 μm (Drossart et al., 2007a, 2007b; Piccioni et al., 2009). The instrument had an imaging capability allowed to cover large areas in a single observation with a good spatial resolution. The FOV of one pixel was 250 μrad (0.0145°). The spectrometer was collecting imaging cubes of 256 × 256 pixels in spatial directions and 432 spectral bands (or wavelengths). The instrument worked as a push-broom spectrometer: one frame was composed of 256 spectra along the slit, and the set of frames was scanned by a mirror or spacecraft motion. The complete data cube covering the 64-mrad FOV required around 50 min if one frame exposition was 8 s. The minimal exposure time of 300 ms is at least 3 times longer than the same parameter used in SPICAV observations. This difference in exposure time is negligible for observation of the O_2 ($a^1\Delta_g$) airglow that mainly varies on a timescale of hours (Alien et al., 1992).

The principal difference in the O_2 ($a^1\Delta_g$) airglow intensity retrieval between SPICAV IR and VIRTIS-M spectra was related to the different spectral resolution and sampling of both instruments. The spectral step of VIRTIS-M was 10 nm, and the full width at half maximum of its point-spread function was about 15 nm. The retrieved O_2 airglow spectra from SPICAV IR dataset are integrated along the wavelengths to retrieve the intensity (Eq. 3). In the VIRTIS spectra, the nightglow signal is not resolved, and it was superimposed to the 1.28-μm transparency window. The 1.18-μm window radiance scaled by an empirical value was used to remove the thermal contribution in order to obtain the O_2 emission spectrum. To this purpose the ratio between integrated emissions of 1.18-μm and 1.28-μm windows was used, whose variations were mainly determined by temperatures of the emitting column, thus, by the topography, and a weak dependence on cloud structure. As a result, ~30 % of 1.18-μm window radiance was removed from the measured signal of the 1.28-μm transparency window.

The VIRTIS-M spectrometer was working from May 2006 until October 2008. A good local time coverage of the Southern Hemisphere was achieved by the VIRTIS nadir measurements. Limb observations performed by VIRTIS partially filled the Northern Hemisphere (Soret et al., 2014). There were several sessions planned in which SPICAV and VIRTIS instruments performed simultaneous observations at the same locations of the Venus globe. The absolute calibration of SPICAV IR in flight was independent of VIRTIS-M (Korablev et al., 2012), thus, it is possible to perform a cross-validation of two instruments' spectra. The VIRTIS-M dataset was analyzed independently in the works by Soret and Gérard (2015) and Shakun et al. (2023). The main difference was in the method used to determine the ratio between the intensity of the 1.18 μm and 1.28 μm windows. In the first approach, empirical value from the airglow-free observations was obtained, which was confirmed by the synthetic thermal radiation spectra. The method is described in Piccioni et al. (2009). The second approach is presented in Shakun et al. (2023). Ratio parameter is defined as a function of topography altitude. Shakun et al. (2023) concludes that the uncertainty of the oxygen extraction by the second method is reduced to 2–3 % instead of 15–20 % with the first algorithm presented in Piccioni et al. (2009).

We have selected 39 VIRTIS-M frames of 35 orbits with successful retrieval of O_2 ($a^1\Delta_g$) airglow from Soret and Gérard (2015) to compare with simultaneous SPICAV IR measurements. In these observations, the SPICAV footprint diameter varied from 21′ at the 47°N latitude to 13° at latitudes farther south than 55°S. VIRTIS data have been arranged in longitude-latitude maps with a grid of 1° in each direction, where values within one bin were averaged. Majority of the observations by both spectrometers do not have full intersection. We average brightness values obtained by VIRTIS-M only over the bins intersected by the SPICAV footprint for the comparison. SPICAV IR airglow observations have also been compared with non-simultaneous observations by VIRTIS-M during twelve Venus Express orbits studied in Shakun et al. (2023). SPICAV IR and VIRTIS-M measurements were taken at the same orbit with a time difference from 2.5 to 11.5 h apart.

The summary of the considered observations is shown in Fig. 3. In general, both experiments lead to similar results, and the same behavior of the airglow is retrieved. The linear correlation coefficient of datasets composed by simultaneous observational sessions is 0.84. Similar linear correlation coefficient of 0.88 is obtained for datasets composed by colocated but non-simultaneous measurements. An example of a simultaneous session (#346) is presented in Fig. 4 where a bright oxygen emission spot was detected by both instruments near the equator at 23.62H of local time. Comparison of raw spectra is presented in the Supplementary material in Fig. S3.1. The brightness values retrieved from both datasets are in good correspondence considering the resulting uncertainty computed from SPICAV IR spectra. On average, values obtained from the VIRTIS dataset are 20 % lower than ones by SPICAV IR. The difference between retrieved values is more pronounced for weak emission. However, both instruments agree regarding the airglow behavior, which is considered in detail in Supplementary material in Figs. S3.2–3.3.

We have established several reasons for the discrepancy, in addition to the shifts of the observed areas. Airglow signals close to the VIRTIS detection limit could appear dimmed in intensity. If VIRTIS-M observations having exposure time of more than 3 s are considered, the correlation between the SPICAV IR and VIRTIS datasets increases to 0.94 (Fig. 3). Instead, even with noisy spectra, the spectral resolving power of SPICAV IR allows robust identification of airglow spectral features in these cases. We also have to take into account that accuracy of the resulting SPICAV's absolute calibration was estimated to be within 20 % interval for all pairs of exposure times and gain values (Korablev et al., 2012). Furthermore, the O_2 ($a^1\Delta_g$) airglow spectra observed in the SPICAV experiment exhibit a minor systematic discrepancy compared to the modeled ones (Section 3.3). In the VIRTIS observations, the 1.18- and 1.2-μm transparency windows are observed simultaneously, but it should be noted that the values of water vapor in the deep atmosphere are obtained with uncertainty. It is determined by inaccurate CO_2 continuum and unknown surface emissivity (Fedorova et al., 2015) and affects the brightness ratio of the 1.18-μm and 1.28-μm windows. Apparently, the most valuable finding is the confirmation of the observed nightglow behavior in all joint observations.

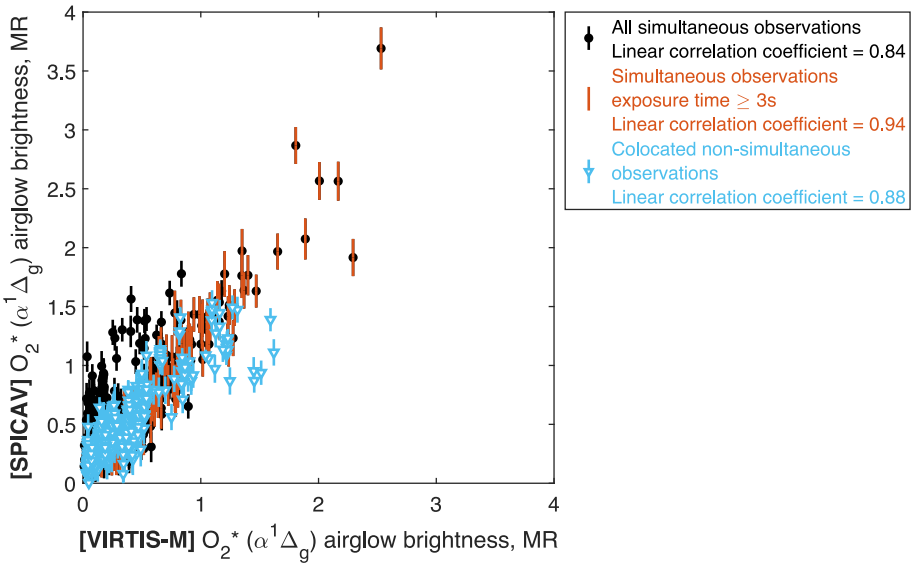

Fig. 3. SPICAV individual measurements of O_2 ($a^1\Delta_g$) airglow intensity versus simultaneous VIRTIS-M observations averaged over the SPICAV footprint. Black circles correspond to simultaneous observations (Soret and Gérard, 2015) by VIRTIS-M, and red dots mark among them exposure times greater than 3 s. Blue triangles correspond to the closest in time observations (Shakun et al., 2023). (For interpretation of the references to colour in this figure legend, the reader is referred to the web version of this article.)

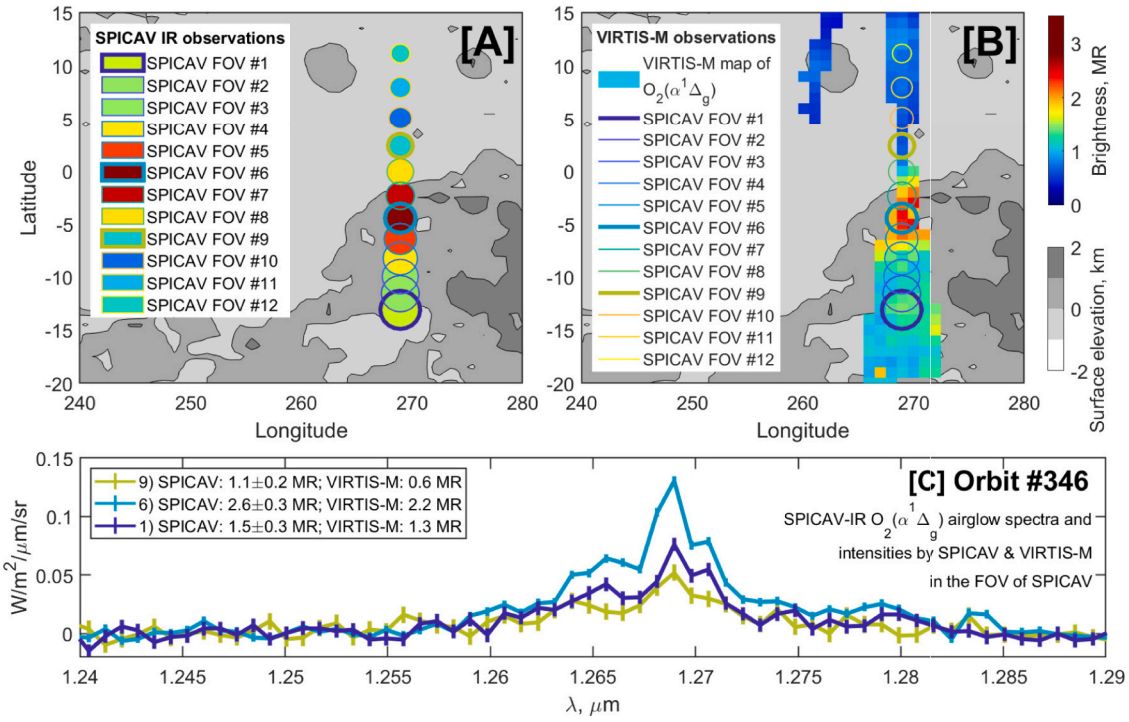

Fig. 4. Comparison of O_2 ($a^1\Delta_g$) airglow observations by SPICAV and VIRTIS during orbit #346 (2 April 2007) by (A) SPICAV IR and (B) VIRTIS-M instruments. Each circle represents a single SPICAV footprint at wavelengths from 1.263 μm to 1.275 μm. Circle fill colors in Panel A represent the brightness measured by SPICAV IR. Circle contour colors in Panels A and B represent SPICAV IR footprint in individual measurements. (C) SPICAV IR retrieved O_2 ($a^1\Delta_g$) airglow spectra. For clarity, only three example spectra are shown. Spectrum colors represent SPICAV-IR measurements marked as circles on the geographical map.

5. Results and discussion

5.1. Radiance map of the Venus night side

The nadir spectra obtained for 8 years, from April 2006 to December 2014, by SPICAV IR/VEx with the SZA higher than 95° were processed in order to separate the O_2 ($a^1\Delta_g$) airglow signal from the contamination by the Venus thermal emission as described in Section 3. The total number of selected spectra (see Section 2) amounts to 8290 from 750 observational sessions (Fig. 1) obtained with emission angle <5°. The corresponding local solar time coverage is from 18H46 to 5H36.

Since variations in the footprints of SPICAV are significant, the global distribution of O_2 ($a^1\Delta_g$) airglow is binned by 0.5 h of local time and 5° of latitude. More detailed grid results in a global distribution

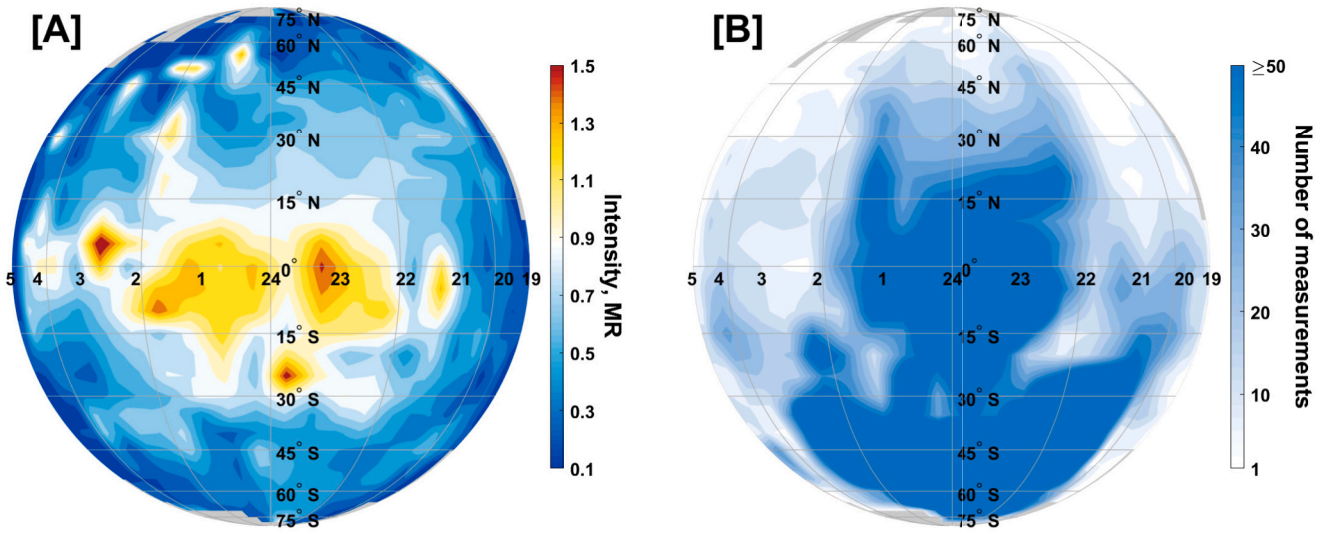

Fig. 5. (A) Average map of oxygen airglow brightness obtained by nadir measurements of SPICAV IR in the night side. The observations are binned on a grid of 30 min in local time and 5° in latitude. (B) The corresponding observation counts.

biased by short-term fluctuations of the emission, especially in the Northern Hemisphere due to a small footprint. Statistics of 50 and more observations in one bin have been achieved in the Southern Hemisphere and around the anti-solar point (Fig. 5B). Fewer observations were conducted at SZA < 150° in the Northern Hemisphere (Fig. 5B). Thus, the bright area of 1.5 MR around 2H30 of local time and 5° N of latitude is caused by a bright spot that persisted from 14 to 16 October 2013 at 5–9° N and 22–25° longitude. It is unlikely to represent the long-term pattern of the emission.

The nightglow pattern is nearly symmetrical around the antisolar point. An intensity maximum of 1.4 MR with a standard deviation of 0.8 MR was found around 23H30 of local time and 0–5° N of latitude. A similar value of 1.6 MR was obtained by Soret et al. (2012) in 2006–2008. The high value of standard deviation represents the variability of the emission brightness around midnight. Towards the terminators, the standard deviation of mean data on the selected grid decreases by 3–4 times. A high variability of the nightglow has been revealed before by various studies reporting its change of 20 % in a timescale of hours (Alien et al., 1992) often vanishing within several days (Alien et al., 1992; Crisp et al., 1996) or local intensities reaching 5–6 MR (Crisp et al., 1996; Ohtsuki et al., 2005; Soret et al., 2014). Similar behavior was observed by SPICAV IR. For instance, during the session #0343A17 the airglow changes from 0.5 ± 0.2 MR to 3.7 ± 0.2 MR along the longitude of 265°. The values reach 5.0 ± 0.1 MR measured on the 1st of April 2011 at 8° N of latitude, 90° of longitude and 23H42 of local time.

The detection limit of O_2 ($a^1\Delta_g$) airglow signal is estimated equal to 0.13 MR on average. It is defined by a non-zero residual of ~0.01 W/m^2/μm/sr in the maximum and the right wing of the 1.28-μm transparency window which likely relates to uncertainties of the model or the AOTF function wings.

A median value of 0.51 ± 0.44 MR over the planet night side for 8 year is practically the same as obtained from VIRTIS data: 0.52 MR by Piccioni et al. (2009) or 0.50 MR by Soret et al. (2012), and as 0.55 MR from ground-based observations (Krasnopolsky, 2010). Our value is still slightly higher than 0.36 ± 0.3 MR obtained by Shakun et al. (2023). Interestingly, an attenuation of the airglow was found at the midnight location, with the brightness increasing to 1H00 of local time. Latitudinal shift of ~10° to the north obtained by VIRTIS-M (Shakun et al., 2010; Soret et al., 2012; Shakun et al., 2023) in nadir and by the limb observations (Soret et al., 2012) is not confirmed by our data. The reason for this difference with the VIRTIS-M result is unclear, but it may be a consequence of sparser coverage in 0–20° N of latitude by VIRTIS-M. Moreover, VIRTIS-M observed these latitudes at high emission angles that increases the retrieval uncertainties. It should be noted that the statistical map accumulated by SPICAV IR in 2006–2008 does not indicate this latitudinal shift, even when measurements performed with larger footprints and emission angles are taken into account (Fig. S4.1 A in the Supplementary material). The importance of data selection bias while observing the variable region of 90–110 km is noted and discussed in the following section. In general, the emission occurs between 22H00 in the evening and 2H00 in the morning at latitudes of 15°S-15°N. Then, the brightness decreases significantly from 22H00 towards the evening terminator. Brighter patches were observed towards the morning terminator. Nevertheless, the airglow decreases gradually towards high latitudes. The SPICAV IR results are consistent with the SSAS circulation pattern; this regime is the main driver of the O_2 ($a^1\Delta_g$) airglow distribution.

5.2. *Data selection bias for the nightglow distribution*

The selection bias of the obtained nightglow distribution was discussed in Section 4 when comparing our results with the VIRTIS dataset. Section 5.1 presents the result of nadir observations. The statistics can be extended by including observations with emission angles up to 60°. We limited the footprint by 3000 km, and the considered values were corrected accounting for the O_2* layer curvature. This restriction also allows us to maintain the assumption of plane-parallel geometry for thermal emission modeling. In the Northern Hemisphere, 95 % of observations have their footprint diameter less than 500 km. In the Southern Hemisphere, ¾ of the all observations encompass an area greater than 500 km in diameter, and the footprint grows towards the South Pole.

Considering larger emission angles extends our dataset to 22,800 spectra. Fig. 1 illustrates the coverage achieved. Results are binned by 0.5 h of local time and 5° of latitude (Fig. 6) similarly to Fig. 5. As the number of observations with a large spatial footprint increases (Fig. 6B), the small features of the O_2 ($a^1\Delta_g$) airglow in the Southern Hemisphere are smoothened. The correction for the atmospheric curvature of the observed O_2 ($a^1\Delta_g$) airglow layer is applied as it is described in Section 3.3. In contrast, the nightglow statistical distribution in the Northern Hemisphere remains fine-structured. However, the local maxima

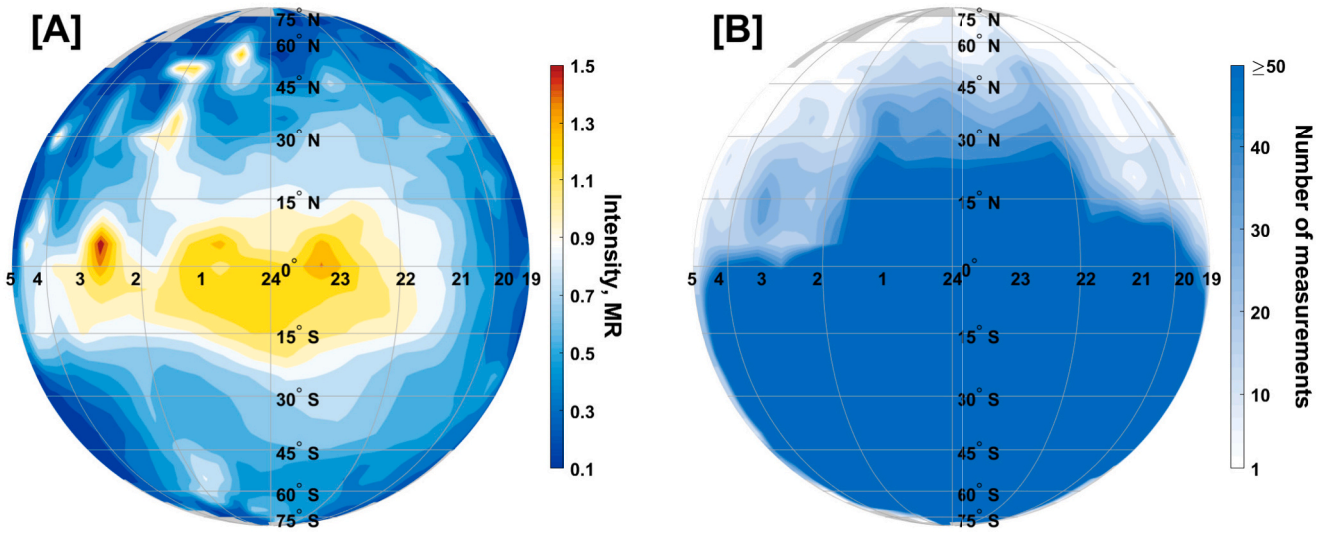

Fig. 6. (A) Average map of oxygen airglow brightness obtained from SPICAV IR measurements conducted with emission angles up to 60° and footprints up to 3000 km. The observations are binned on a grid of 30 min in local time and 5° in latitude. (B) The corresponding observation counts.

obtained may be influenced by other factors, such as short-term changes. The bright area of 1.5 MR around 2H30 of local time and 5° N of latitude (Fig. 5A, 6A) is an example of such a bias, as it was discussed in Section 5. The distribution of points by local time for selected latitude ranges is presented in detail in the Supplementary material (Fig. S5.1–5.4).

The entire SPICAV IR dataset confirms the prominent global maximum in proximity to the antisolar point. An intensity of 1.3 MR with a standard deviation of 0.6 MR was found at 23H30 of local time and 0–5° N of latitude. The similar value 1.3 ± 0.8 MR is obtained at 5–10° N of latitude and 23H30 of local time.

Fig. 7 presents detailed comparison of the data selection bias. In the Northern Hemisphere, the data coverage is not significantly improved due to the small footprints, and the local time trend remains almost unchanged while averaging more measurements. In contrast, the general local time trend is confirmed by the extended data coverage in the Southern Hemisphere. The insertion of measurements leads only to a regularization of the trend: the bright feature (20–25° S at the midnight) obtained for nadir measurements disappears.

5.3. *Bright spots distribution*

Nightglow intensities of 3–5 MR, higher than the global maximum of 1.4 MR found around 23H30 of local time and 0–5° N of latitude (Fig. 5), are occasionally observed. Such values were noted in ground-based

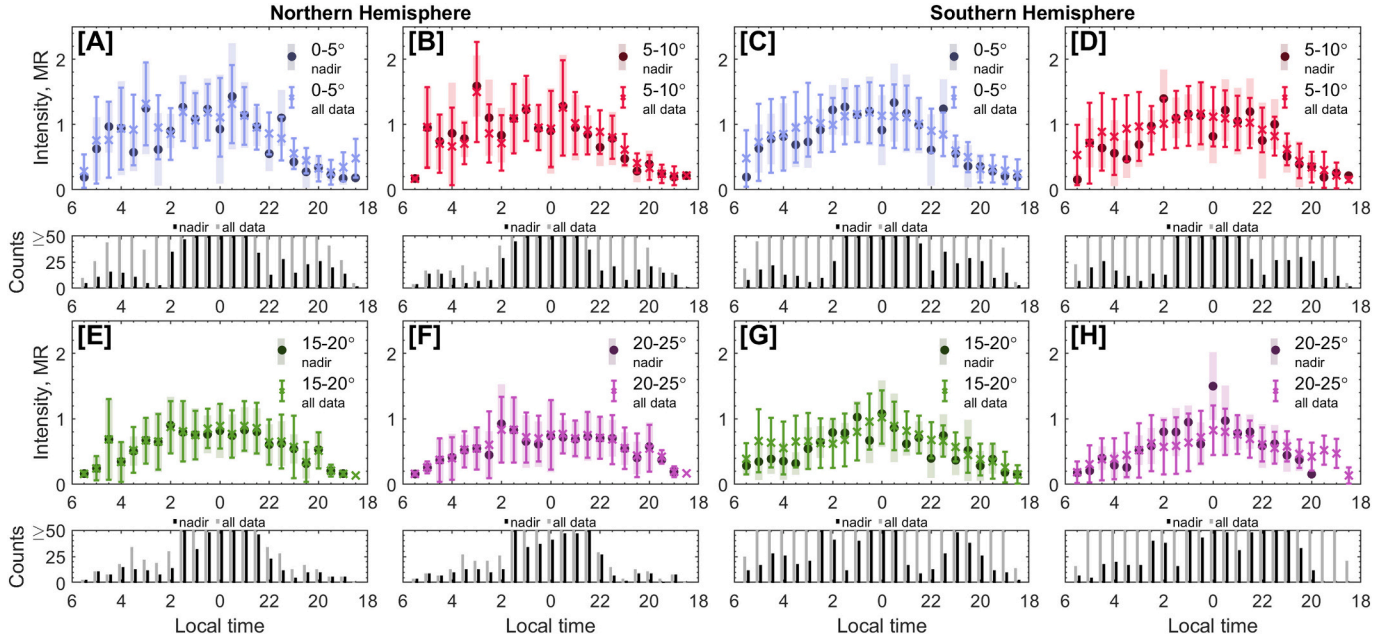

Fig. 7. Detailed comparison of averaged airglow radiance maps presented in Figs. 5 and 6. The observations are binned on a grid of 30 min in local time and 5° in latitude. Circles with wide errorbars represent the data of Fig. 5 obtained for the emission angles <5°. Crosses with thin errorbar lines show the values of Fig. 6 (emission angles <60°, SPICAV IR footprints up to 3000 km) for the same latitude ranges. Average values are presented with the standard deviation. Panels A, B, E, F correspond to the Northern Hemisphere, and Panels C, D, G, H correspond to the Southern Hemisphere. Bar plots represent the number of observations in one bin. Black bars correspond to emission angles <5°. Gray bars correspond to emission angles <60° and SPICAV IR footprints <3000 km.

(Crisp et al., 1996; Ohtsuki et al., 2005, 2008a) and VIRTIS-M observations (Shakun et al., 2023). It was also showed that bright O_2 ($a^1\Delta_g$) spots occur up to polar latitudes on the Venus night side (Alien et al., 1992; Crisp et al., 1996; Gérard et al., 2014; Soret et al., 2014) while the brightest emissions concentrate around the anti-solar point (Soret et al., 2014). Its appearance at high latitudes however implies that the SSAS is perturbed by transient effects (Soret et al., 2014) influencing a direct flow from the subsolar to the anti-solar point with short-term variability.

Within the SPICAV IR dataset, 5 % of measurements exceed the global maximum of 1.4 MR. This threshold is used to determine "bright spots" of the nightglow. A strong increase in the airglow reflects dramatic perturbations in atomic oxygen downward flux or in atmospheric density. Thus, a pattern of such events should be informative for establishing the impact domain of air transport change. Statistically, bright spots occurred with greater frequency in Area 1, which is highlighted in Fig. 8B and encompasses a local time range from 22H00 to 2H00 and latitudes of 15°S-15°N. However, these phenomena were observed all over the nightside at latitudes below 70° (Fig. 8B). It should be noted that only a few isolated cases showed intensity exceeding 3 MR.

The geographical distribution of bright spots (Fig. 8D) does not match any of the features of the underlying surface. The obtained overall distribution is fairly uniform in longitude and symmetrical in latitude (Fig. 8D). Area 2 which is highlighted in Fig. 8D was investigated in detail. It encompasses longitudes of 0–120° and 180–360° and latitudes of 10°S-10°N, where an increase in the number of bright spot detections was observed. The majority of these cases (81 %) correspond to local times from 22H00 to 2H00. Additionally, 5 % of these observations are in the local time range of 20-22H, while 14 % of equatorial bright spots are in the local time range of 2-5H. There is no obvious relation with longitude for neither of these cases. Bright spot detections in the Northern Hemisphere in the 0–120° of longitude and in the Southern Hemisphere in the 180–300° of longitude outside the Area 2 (Fig. 8D) are also related to the observed local times rather than longitudes: the measurements are in the proximity of the midnight meridian.

The bright spots local time distribution closely follows the average map of the nighttime hemisphere (Fig. 8B). First, most of them were observed near the anti-solar point within ±2 h of local time and ± 15° of latitude (Area 1, Fig. 8B). The bright spots were not observed above 70° of latitude, neither in the Northern nor in the Southern Hemispheres. A possible feature of this distribution is that the brightest airglow appeared 35 % more often towards the morning terminator, taking into account the total number of observations in 2-6H and 18-22H of local time.

5.4. Short-term variations

O_2 ($a^1\Delta_g$) nightglow is highly variable in short time scales. Venus PCM (Navarro et al., 2021) pointed out that Kelvin waves occurring at cloud tops should cause a shift in O_2 ($a^1\Delta_g$) airglow patch to higher latitudes from the equator and its intensity variations within a period of ~5 days. Venus PCM predicts the phase lag between the O_2 ($a^1\Delta_g$) brightness and cloud top reflected radiance of ~1.4 days, corresponding to one-fourth of the Kelvin wave period (Navarro et al., 2021). Venus Monitoring Camera (VMC) on board Venus Express (Markiewicz et al.,

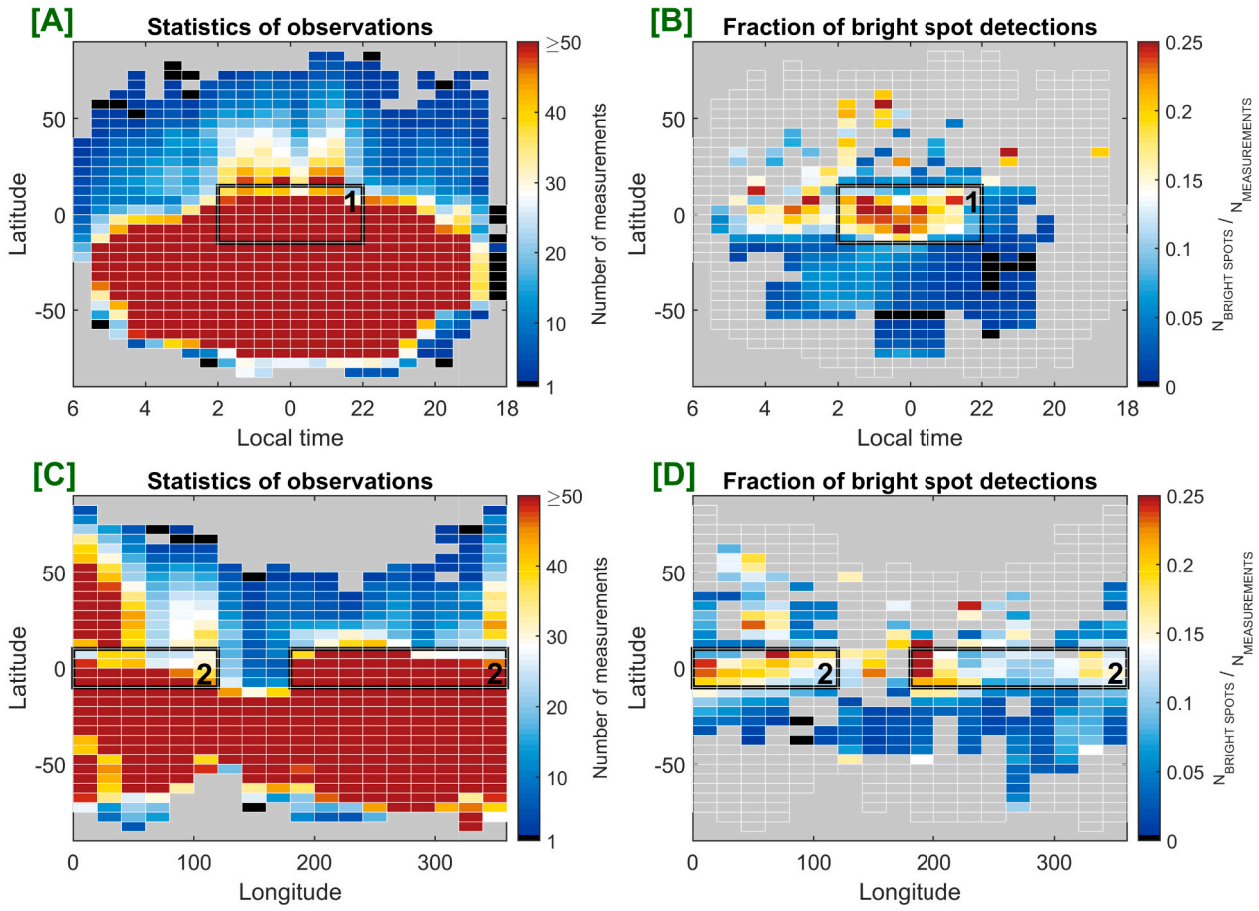

Fig. 8. Panels A, C represent the full statistics of observations. Panels B, D show the statistics of bright spots (≥ 1.4 MR) detections. White lines at the panels indicate bins covered by SPICAV IR. One bin size is 5° of latitude and 0.5 h of local time for latitude-local time coverage in panels A-B and 5° of latitude and 20° of longitude for latitude-longitude coverage in panels C—D. Areas 1 and 2 are highlighted due to a sufficient number of observations and an increased number of detected bright spots.

2007) observed a similar periodicity of 4–5 days of the ultraviolet reflectivity and wind field at cloud tops in orbit range of 436–490 (Nara et al., 2019) from the 1st of July to the 28th of August in 2007. The periodicity of UV reflectivity was obtained at 10°S after averaging within the local solar time range of 11H00—13H00 (Nara et al., 2019). On the same dates, SPICAV IR observed the O_2 ($a^1\Delta_g$) nightglow distant from the equator at latitudes from 60° to 30° S. Airglow intensities obtained by SPICAV IR are averaged for 1 day and 30–60° S latitude range. Observations conducted during one orbit spanned a narrow local time range. The observed local time intervals of several sequential orbits intersected and ranged from 21H00 to 03H00. The brightest patch was detected at 40° S of latitude during the session #0479 (Fig. 9A-B) and diminishes ~2 days later. Following the result by Nara et al. (2019) the radiance reflected by clouds at 10°S averaged over the local time range of 11H00—13H00 reaches its minimum at orbit #0479. The shift between the O_2 ($a^1\Delta_g$) brightness minimum (orbit #481, Fig. 9A) and cloud top reflected radiance is ~2 days in this case. In contrast, the phase shift between periodical variations of the cloud top brightness and day-side OII EUV emission at 135.6 nm was 4 ± 2 h (Nara et al., 2020).

A Lomb-Scargle periodogram was computed for the entire set of observations from orbits #436–490 (Fig. 9A, B). To evaluate the statistical significance of the identified periodogram peaks, the false-alarm probability (FAP) threshold was determined. The FAP represents the probability of false detection of periodicity. It can be observed in Fig. 9C that the most prominent periodogram peak occurs at the period of 5.2 days. However, the FAP threshold which is lower than this peak corresponds to a false-detection probability of 60 %. Consequently, no periodicity can be concluded from the airglow measurements. It is also difficult to directly compare our O_2 ($a^1\Delta_g$) intensity variations and the VMC results at the cloud tops (Nara et al., 2020) because of the large local time spread of SPICAV observations (Fig. 9B).

Consecutive observations covering similar latitudes, longitudes, and local time ranges are now considered in detail. Seven groups (Fig. 10, Figs. S6.1–6.6 in the Supplementary material) of such sessions are found in the SPICAV IR dataset. Due to a small footprint in the Northern Hemisphere, and, thus, a sparse coverage, the chosen sequences correspond mostly to Southern Hemisphere observations. The short-term periodical fluctuations are retrieved for these groups using the Lomb-Scargle periodogram. The significance of periodogram peaks is evaluated using the FAP threshold. The only sequence for which the detection probability exceeds 75 % is presented in Fig. 10. This sequence corresponds to the orbits #2564–2583 from the 28th of April to the 17th of May in 2013. The values demonstrate fluctuations with a period of 5.4 days. In other examples (see Figs. S6.1–6.6), periodicity cannot be definitively determined.

5.5. Comparison with solar activity

The Venus Express mission covered 2.5 years of the 23rd Solar cycle and 6 years of the 24th Solar cycle. The period corresponds to almost a whole 11-year Solar cycle, allowing to search for a possible link between the EUV solar flux and the airglow brightness variations. The radio emission flux at 10.7 cm, i.e., the $F_{10.7}$ index (https://spaceweather.gc.ca/forecast-prevision/solar-solaire/solarflux/sx-5-mavg-en.php), is usually used as a proxy for EUV in the solar EUV irradiance models (Richards et al., 1994; Tobiska et al., 2000). Both emissions originate from the solar corona and are highly correlated in time, however, the link is not invariant. In the solar minimum of 2008–2009, the EUV flux dropped lower than in 1996 at the end of the 22nd Solar cycle for the same $F_{10.7}$ index (Chen et al., 2011). Thus, we use the EUV solar flux at 0.1–50 nm measured by the Solar EUV Monitor (SEM) aboard the Solar Heliospheric Observatory (SOHO) satellite at 1 AU (Judge et al., 1998). The flux index is equivalent to 10^{10} photons/cm^2/s. Data on the EUV daily fluxes averaged over the full solar disk is available from the Space Sciences Center of the University of Southern California (https://dornsifecms.usc.edu/space-sciences-center/download-sem-data/). The $EUV_{0.1–50}$ values are provided for the Earth, while the flux EUV_{Earth} is provided for a given time t (Eq. 5). Taking into account the offset between Venus and Earth positions, the date shift ΔT should be accounted for. The time shift in Earth days is computed according to Eq. 4.

$$\Delta T = 27\,\frac{\Delta\lambda}{360},\ -180 \le \Delta\lambda \le 180 \tag{4}$$

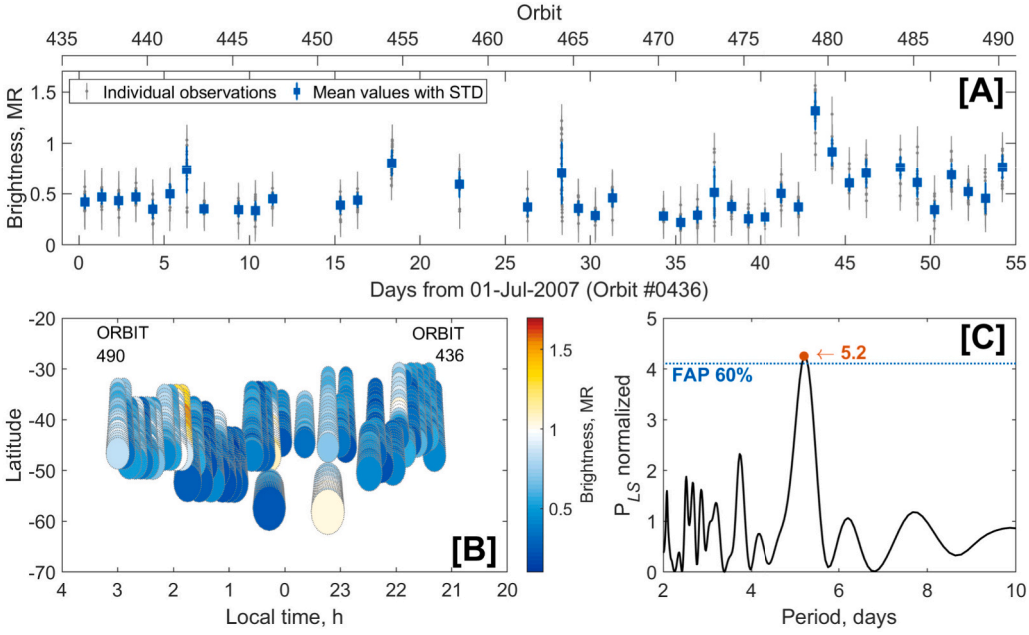

Fig. 9. Short-term O_2 ($a^1\Delta_g$) variations from the 1st of July to the 28th of August in 2007 (orbits #436–490). (A) Timeline of variations with the period of 5.2 days defined by Lomb-Scargle periodogram. (B) Overview of observation distribution with the SPICAV footprints. (C) Lomb-Scargle periodogram for the mean values of observations binned by 1 day. The periodogram is normalized by a factor of two times the variance of the dataset. The blue dotted line represents the threshold of a false-alarm probability of 60 %. The peak exceeding the computed FAP threshold is highlighted by the red dot. (For interpretation of the references to colour in this figure legend, the reader is referred to the web version of this article.)

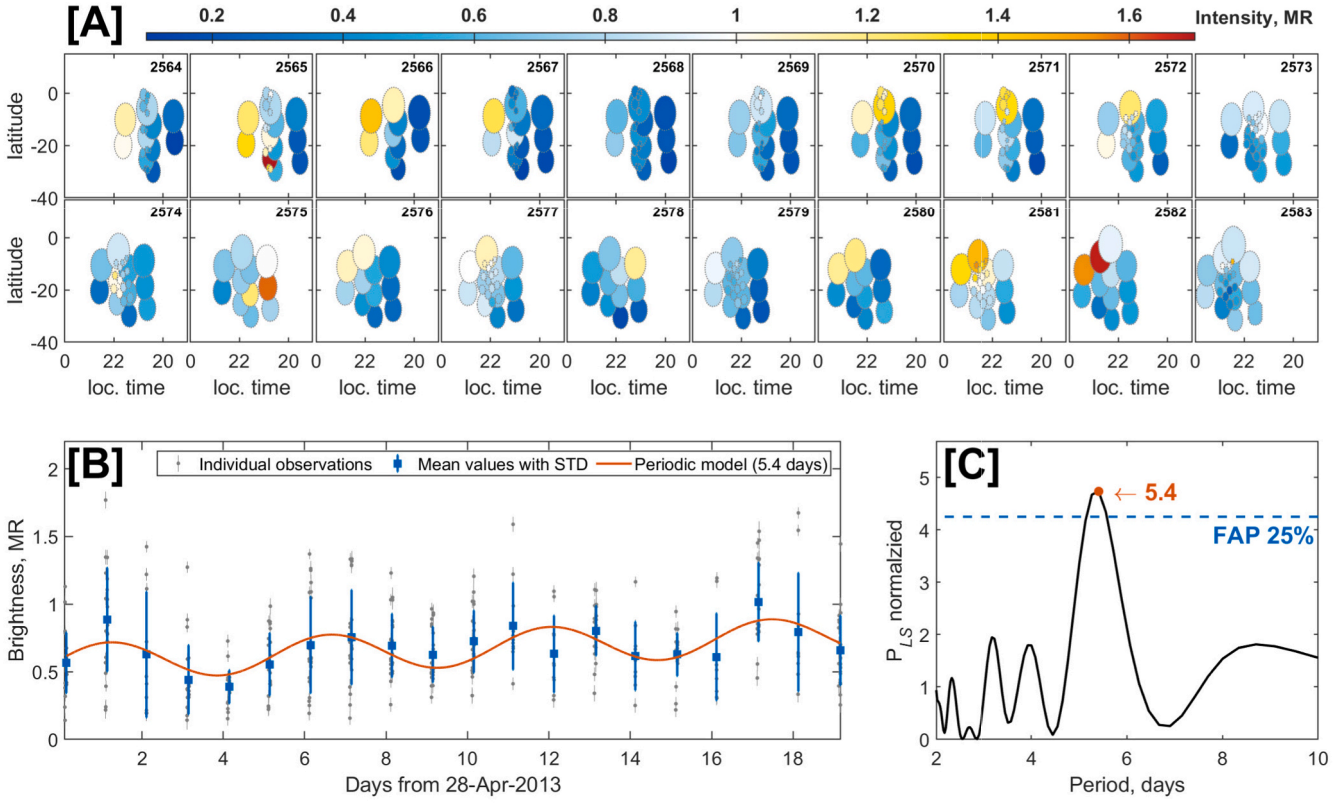

Fig. 10. Short-term O_2 ($a^1\Delta_g$) variations from the 28th of April to the 17th of May in 2013 (orbits #2564–2583). (A) Overview of observations with the SPICAV footprints. (B) Timeline of variations and possible periodic function with the period of 5.4 days defined by Lomb-Scargle periodogram. (C) Lomb-Scargle periodogram for the mean values of observations binned by 1 day. The periodogram is normalized by two times the variance of the dataset. The blue dotted line represents the threshold of a false-alarm probability of 25 %. The peak exceeding the computed FAP threshold is highlighted by the red dot. (For interpretation of the references to colour in this figure legend, the reader is referred to the web version of this article.)

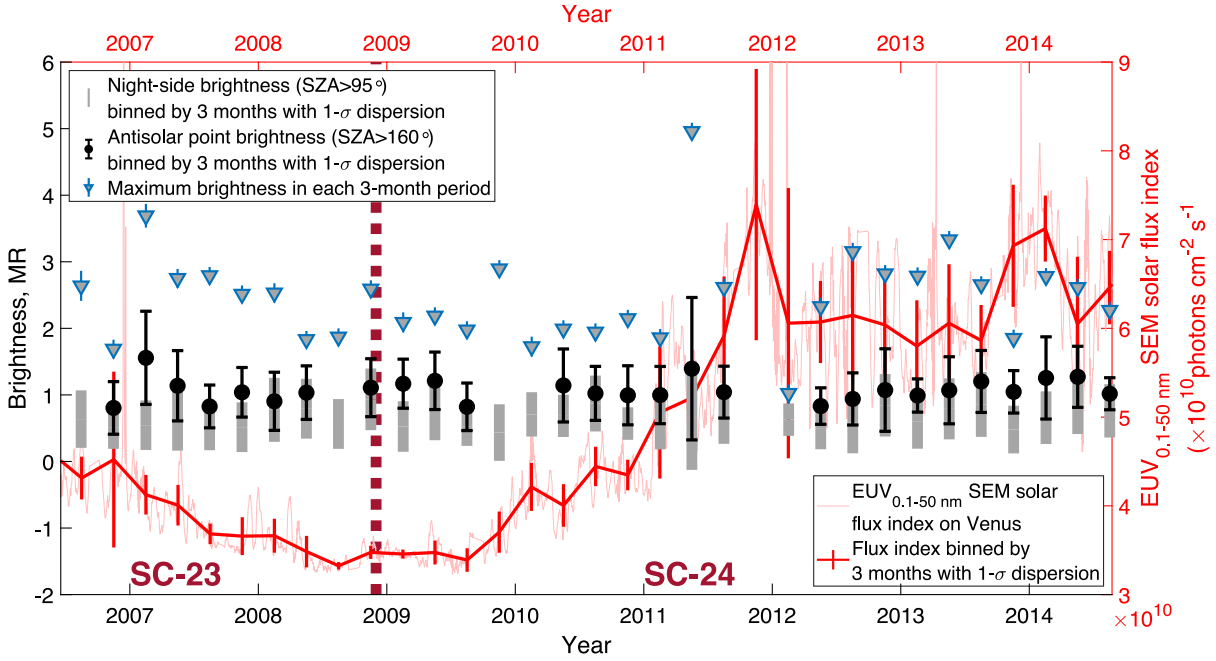

Fig. 11. O_2 ($a^1\Delta_g$) SPICAV brightness compared to solar EUV flux. Black dots are antisolar point brightness (SZA > 150°) binned by 3 months represented with the standard deviation of values in one bin. The gray bars correspond to the average of all night-side observations binned by 3 months with standard deviation. The blue triangles represent the airglow maximum in each 3-month period. The light red curve is SOHO-CELIAS/SEM (Judge et al., 1998). EUV daily average at 1 AU recomputed for Venus. The red curve represents the solar flux index binned by 3 months with standard deviation. The 23rd Solar cycle ended in December 2008. (For interpretation of the references to colour in this figure legend, the reader is referred to the web version of this article.)

where 27 days is the Sun rotation period, $\Delta\lambda$ is the difference between Venus and Earth solar longitudes in degrees and should be in the range between -180° and 180° for estimation of the closest available data. Therefore, the EUV flux on Venus EUV_{Venus} is computed by Eq. 5.

$$EUV_{Venus} = \frac{R^2{}_{Venus}}{R^2{}_{Earth}} \times EUV_{Earth}(t + \Delta T) \quad (5)$$

The $EUV_{0.1–50}$ index decreased from 4.4 to 3.3 in 2006–2009 and then reached 7 at the end of 2011 and 7.1 in the beginning of 2014, that is, 2.1 times higher than in the minimum. The 24th Solar cycle actually differs from previous cycles by a lower level of activity and a deep minimum in 2008 (Solomon et al., 2010; Woods et al., 2022). For instance, the maximal index of the 23rd Solar cycle was 13.5 (Soret et al., 2012).

Fig. 11 shows the obtained O_2 ($a^1\Delta_g$) brightness compared to the solar EUV flux. An individual session of measurements by SPICAV covers usually a small fraction of the night side, so the results were binned by 3 months and averaged in each bin. Such long-term sequence of mean intensities is computed for all the observations regardless of their location or for the observations located around the antisolar point with SZA $> 150^\circ$. The $EUV_{0.1–50}$ index was also smoothed in the same way. Fig. 11 shows the obtained long-term dependencies representing the 3-month averaged value with the standard deviation. The antisolar point intensity is 1–2.7 times larger than the night-side average, as expected. The strong variation within one time range of three months is prevailed, therefore, any particular trend of O_2 ($a^1\Delta_g$) airglow intensity is not pronounced. Linear correlation coefficient of long-term average intensity dependencies and 3-months mean $EUV_{0.1–50}$ index is equal to -0.1339 for the antisolar brightness and to -0.0244 for the night-side average.

Soret and Gérard (2015) did a similar analysis of the VIRTIS observations. The instrument was working from May 2006 to October 2008 which was the phase of the deep solar minimum. The $EUV_{0.1–50}$ index decreased from 4.4 to 3.3 for this time range. A hint of a positive correlation of the solar flux and the peak intensities was found, and the linear correlation coefficient was equal to 0.62. However, the correlation coefficient calculated for brightness averaged over the entire night side was only 0.35. Therefore, no link between the solar activity and the O_2 ($a^1\Delta_g$) airglow was established. The SPICAV IR observations of peaking intensities also do not reveal any evident correlation with solar EUV. The monitoring by SPICAV IR confirms this conclusion for either the peak intensity, the antisolar or the overall O_2 ($a^1\Delta_g$) brightness.

The $F_{10.7}$ index recalculated for Venus varied from 140 to 120 at the end of the 23rd Solar cycle and from 120 to 200–250 in the 24th Solar cycle. Bougher and Borucki (1994) studied a difference in O_2 ($a^1\Delta_g$) peak intensity for three solar activity scenarios: solar flux with $F_{10.7} = 70$ (minimum), $F_{10.7} = 150$ (medium) and $F_{10.7} \geq 200$ (maximum). There was no influence on temperatures of the Venus night side (Bougher and Borucki, 1994). A similar conclusion about the night exosphere temperature has been drawn by the recent simulations, showing a greater influence of non-orographic gravity waves than solar activity on model results (Martinez et al., 2023). The peak intensities of VTGCM simulated O_2 ($a^1\Delta_g$) airglow are equal to 0.49, 0.54 and 0.70 MR for three solar flux conditions respectively, suggesting a minor correlation with solar activity (Bougher and Borucki, 1994). In our work, we conclude that the observed daily variations are much more significant, and that this variability is likely related to dramatic changes in the wind field that can be driven by solar activity among other sources. The lack of imaging capabilities interferes with the correlation analysis on a daily basis, since only a small area is usually scanned.

6. Conclusions

Here we reported a complete set of SPICAV IR observations of O_2 ($a^1\Delta_g$) nightglow lasting from the beginning of 2006 till the end of the Venus Express mission in 2014. This study analyzes more than 2000 sessions of nadir observations (~20,000 spectra). The well-resolved spectra comprising both the thermal emission and the airglow signals were fit to radiative transfer and oxygen emission models. This approach ensures a robust separation of the airglow intensity from the thermal contamination.

The observed intensities vary between the detection limit estimated at 0.13 MR and the peak value of 5.0 ± 0.1 MR. The infrared O_2 ($a^1\Delta_g$) airglow driven by the subsolar to antisolar circulation occurs between two global circulation regimes: cloud super-rotation below 90 km and the subsolar to antisolar circulation over 120 km. The local time and latitude average distribution of the O_2 ($a^1\Delta_g$) airglow at night was obtained. It confirms that the global maximum with an intensity of 1.4 ± 0.8 MR is near the anti-solar point. Median value over the planet's night side is 0.51 MR. In general, the distribution is fairly symmetrical about the equator.

In 2006–2008, VIRTIS imaging spectrometer on board the Venus Express also performed observation of the O_2 ($a^1\Delta_g$) nightglow (Soret et al., 2014). Comparison with the simultaneous and colocated VIRTIS-M observations was done. In these observations, both instruments retrieve the same behavior of the nightglow. Few deviations in absolute values could be due to uncertainty of the two experiments. The SPICAV average distribution is likewise in good agreement with the analysis of the VIRTIS-M data.

A high variability of the airglow was observed. Spots with intensities exceeding the antisolar average value were observed within a latitude range of 70°S-70°N. The majority of such cases were located in the immediate vicinity of the antisolar point. Towards the morning terminator, they also occur 35 % more often. Short-term nightglow periodicity can be caused by the upward propagation of a cloud-top Kelvin wave. The Venus PCM simulation produced the 5.7-day period of the Kelvin wave and the airglow variations (Navarro et al., 2021). Seven SPICAV IR observation sequences were conducted over a period of 1–2 months covering proximate locations. Only one set of airglow intensity data revealed a 5-day periodicity with a 75 % significance level. The source of observed fluctuations cannot be identified solely based on the SPICAV dataset due to its poor mapping capability.

The full SPICAV IR dataset gathers airglow observations under different solar activity conditions in 2006–2014: from the end of the 23rd Solar cycle to the maximum in the 24th Solar cycle. A correlation between the solar EUV flux (a proxy of CO_2 photo-dissociation rate) and the O_2 infrared emission was previously predicted by global circulation model simulations (Bougher and Borucki, 1994). In our study, the direct link between changes in solar flux and O_2 ($a^1\Delta_g$) airglow intensity was not found against the much more significant short-term fluctuations.

CRediT authorship contribution statement

D. Evdokimova: Visualization, Validation, Software, Methodology, Investigation, Funding acquisition, Data curation, Conceptualization, Writing – review & editing, Writing – original draft. **A. Fedorova:** Supervision, Methodology, Conceptualization, Writing – review & editing. **M. Zharikova:** Software, Writing – review & editing. **F. Montmessin:** Supervision, Project administration, Writing – review & editing. **O. Korablev:** Resources, Project administration, Writing – review & editing. **L. Soret:** Validation, Writing – review & editing. **D. Gorinov:** Validation, Writing – review & editing. **D. Belyaev:** Supervision, Writing – review & editing. **J.-L. Bertaux:** Methodology.

Declaration of competing interest

The authors declare that they have no known competing financial interests or personal relationships that could have appeared to influence the work reported in this paper.

Data availability

Data is available on Mendeley Data under the DOI: https://doi.org/10.17632/8tvbtzpg7h.1.

Acknowledgments

The development of a radiation transfer model for the Venus transparency windows (Section 3.1) and the SPICAV IR data processing (Section 3.3, Section 5) was performed by DE with the financial support by the grant #23-72-01064 of the Russian Science Foundation. LS who performed the VIRTIS-M data processing (Section 4), acknowledges funding by the Belgian Science Policy Office (BELSPO), with the financial and contractual coordination by the ESA Prodex Office (PEA 4000140863). We would like to thank the reviewers for their constructive feedback and valuable comments, which helped us to improve the quality of the manuscript.

Appendix A. Supplementary data

Supplementary data to this article can be found online at https://doi.org/10.1016/j.icarus.2024.116417.

References

Alien, D., Crisp, D., Meadows, V., 1992. Variable oxygen airglow on Venus as a probe of atmospheric dynamics. Nature 359, 516–519. https://doi.org/10.1038/359516a0.

Altieri, F., Migliorini, A., Zasova, L., Shakun, A., Piccioni, G., Bellucci, G., 2014. Modeling VIRTIS/VEX O2(a1Δg) nightglow profiles affected by the propagation of gravity waves in the Venus upper mesosphere. J. Geophys. Res. Planets 119, 2300–2316. https://doi.org/10.1002/2013JE004585.

Bailey, J., Chamberlain, S., Crisp, D., Meadows, V.S., 2008a. Near infrared imaging spectroscopy of Venus with the Anglo-Australian telescope. Planet. Space Sci. 56, 1385–1390. https://doi.org/10.1016/j.pss.2008.03.006. Ground-based and Venus Express Coordinated Campaign.

Bailey, J., Meadows, V.S., Chamberlain, S., Crisp, D., 2008b. The temperature of the Venus mesosphere from O2 (aΔg1) airglow observations. Icarus 197, 247–259. https://doi.org/10.1016/j.icarus.2008.04.007.

Barber, R.J., Tennyson, J., Harris, G.J., Tolchenov, R.N., 2006. A high-accuracy computed water line list. Mon. Not. R. Astron. Soc. 368, 1087–1094. https://doi.org/10.1111/j.1365-2966.2006.10184.x.

Bertaux, J.-L., Nevejans, D., Korablev, O., Villard, E., Quémerais, E., Neefs, E., Montmessin, F., Leblanc, F., Dubois, J.P., Dimarellis, E., Hauchecorne, A., Lefèvre, F., Rannou, P., Chaufray, J.Y., Cabane, M., Cernogora, G., Souchon, G., Semelin, F., Reberac, A., Van Ransbeek, E., Berkenbosch, S., Clairquin, R., Muller, C., Forget, F., Hourdin, F., Talagrand, O., Rodin, A., Fedorova, A., Stepanov, A., Vinogradov, I., Kiselev, A., Kalinnikov, Yu., Durry, G., Sandel, B., Stern, A., Gérard, J.C., 2007a. SPICAV on Venus express: three spectrometers to study the global structure and composition of the Venus atmosphere. Planet. Space Sci. 55, 1673–1700. https://doi.org/10.1016/j.pss.2007.01.016. The Planet Venus and the Venus Express Mission, Part 2.

Bertaux, J.-L., Vandaele, A.-C., Korablev, O., Villard, E., Fedorova, A., Fussen, D., Quémerais, E., Belyaev, D., Mahieux, A., Montmessin, F., Muller, C., Neefs, E., Nevejans, D., Wilquet, V., Dubois, J.P., Hauchecorne, A., Stepanov, A., Vinogradov, I., Rodin, A., 2007b. A warm layer in Venus' cryosphere and high-altitude measurements of HF, HCl, H2O and HDO. Nature 450, 646–649. https://doi.org/10.1038/nature05974.

Bertaux, J.-L., Khatuntsev, I.V., Hauchecorne, A., Markiewicz, W.J., Marcq, E., Lebonnois, S., Patsaeva, M., Turin, A., Fedorova, A., 2016. Influence of Venus topography on the zonal wind and UV albedo at cloud top level: the role of stationary gravity waves. J. Geophys. Res. Planets 121, 1087–1101. https://doi.org/10.1002/2015JE004958.

Bertaux, J.-L., Hauchecorne, A., Lefèvre, F., Bréon, F.-M., Blanot, L., Jouglet, D., Lafrique, P., Akaev, P., 2020. The use of the 1.27 μm O2 absorption band for greenhouse gas monitoring from space and application to MicroCarb. Atmospheric Meas. Tech. 13, 3329–3374. https://doi.org/10.5194/amt-13-3329-2020.

Bézard, B., Fedorova, A., Bertaux, J.-L., Rodin, A., Korablev, O., 2011. The 1.10- and 1.18-μm nightside windows of Venus observed by SPICAV-IR aboard Venus express. Icarus 216, 173–183. https://doi.org/10.1016/j.icarus.2011.08.025.

Bougher, S.W., Borucki, W.J., 1994. Venus O2 visible and IR nightglow: implications for lower thermosphere dynamics and chemistry. J. Geophys. Res. Planets 99, 3759–3776. https://doi.org/10.1029/93JE03431.

Bougher, S.W., Alexander, M.J., Mayr, H.G., 1997. Upper atmosphere dynamics: Global circulation and gravity waves. In: Venus II: Geology, Geophysics, Atmosphere, and Solar Wind Environment. University of Arizona Press, Tucson, pp. 259–291.

Brecht, A.S., Bougher, S.W., Gérard, J.-C., Parkinson, C.D., Rafkin, S., Foster, B., 2011. Understanding the variability of nightside temperatures, NO UV and O2 IR nightglow emissions in the Venus upper atmosphere. J. Geophys. Res. Planets 116. https://doi.org/10.1029/2010JE003770.

Chen, Y., Liu, L., Wan, W., 2011. Does the F10.7 index correctly describe solar EUV flux during the deep solar minimum of 2007–2009? J. Geophys. Res. Space Physics 116. https://doi.org/10.1029/2010JA016301.

Connes, P., Noxon, J.F., Traub, W.A., Carleton, N.P., 1979. O2(1Δ) emission in the day and night airglow of Venus. Astrophys. J. 233, L29–L32. https://doi.org/10.1086/183070.

Crisp, D., McMuldroch, S., Stephens, S.K., Sinton, W.M., Ragent, B., Hodapp, K.W., Probst, R.G., Doyle, L.R., Allen, D.A., Elias, J., 1991. Ground-based near-infrared imaging observations of Venus during the Galileo encounter. Science 253 (5027), 1538–1541. https://doi.org/10.1126/science.253.5027.1538.

Crisp, D., Meadows, V.S., Bézard, B., de Bergh, C., Maillard, J.-P., Mills, F.P., 1996. Ground-based near-infrared observations of the Venus nightside: 1.27-μm O2(a1Δg) airglow from the upper atmosphere. J. Geophys. Res. Planets 101, 4577–4593. https://doi.org/10.1029/95JE03136.

Drossart, P., Piccioni, G., Adriani, A., Angrilli, F., Arnold, G., Baines, K.H., Bellucci, G., Benkhoff, J., Bézard, B., Bibring, J.-P., Blanco, A., Blecka, M.I., Carlson, R.W., Coradini, A., Di Lellis, A., Encrenaz, T., Erard, S., Fonti, S., Formisano, V., Fouchet, T., Garcia, R., Haus, R., Helbert, J., Ignatiev, N.I., Irwin, P.G.J., Langevin, Y., Lebonnois, S., Lopez-Valverde, M.A., Luz, D., Marinangeli, L., Orofino, V., Rodin, A.V., Roos-Serote, M.C., Saggin, B., Sanchez-Lavega, A., Stam, D. M., Taylor, F.W., Titov, D., Visconti, G., Zambelli, M., Hueso, R., Tsang, C.C.C., Wilson, C.F., Afanasenko, T.Z., 2007a. Scientific goals for the observation of Venus by VIRTIS on ESA/Venus express mission. Planet. Space Sci. 55, 1653–1672. https://doi.org/10.1016/j.pss.2007.01.003. The Planet Venus and the Venus Express Mission, Part 2.

Drossart, P., Piccioni, G., Gérard, J.C., Lopez-Valverde, M.A., Sanchez-Lavega, A., Zasova, L., Hueso, R., Taylor, F.W., Bézard, B., Adriani, A., Angrilli, F., Arnold, G., Baines, K.H., Bellucci, G., Benkhoff, J., Bibring, J.P., Blanco, A., Blecka, M.I., Carlson, R.W., Coradini, A., Di Lellis, A., Encrenaz, T., Erard, S., Fonti, S., Formisano, V., Fouchet, T., Garcia, R., Haus, R., Helbert, J., Ignatiev, N.I., Irwin, P., Langevin, Y., Lebonnois, S., Luz, D., Marinangeli, L., Orofino, V., Rodin, A.V., Roos-Serote, M.C., Saggin, B., Stam, D.M., Titov, D., Visconti, G., Zambelli, M., Tsang, C., 2007b. A dynamic upper atmosphere of Venus as revealed by VIRTIS on Venus express. Nature 450, 641–645. https://doi.org/10.1038/nature06140.

Evans, K.F., 2007. SHDOMPPDA: a radiative transfer model for cloudy sky data assimilation. J. Atmos. Sci. 64, 3854–3864. https://doi.org/10.1175/2006JAS2047.1.

Fedorova, A., Bézard, B., Bertaux, J.-L., Korablev, O., Wilson, C., 2015. The CO2 continuum absorption in the 1.10- and 1.18-μm windows on Venus from Maxwell Montes transits by SPICAV IR onboard Venus express. Planet. Space Sci. 113–114, 66–77. https://doi.org/10.1016/j.pss.2014.08.010. SI:Exploration of Venus.

Fukuhara, T., Futaguchi, M., Hashimoto, G.L., Horinouchi, T., Imamura, T., Iwagaimi, N., Kouyama, T., Murakami, S., Nakamura, M., Ogohara, K., Sato, M., Sato, T.M., Suzuki, M., Taguchi, M., Takagi, S., Ueno, M., Watanabe, S., Yamada, M., Yamazaki, A., 2017. Large stationary gravity wave in the atmosphere of Venus. Nat. Geosci. 10, 85–88. https://doi.org/10.1038/ngeo2873.

Gérard, J.-C., Saglam, A., Piccioni, G., Drossart, P., Cox, C., Erard, S., Hueso, R., Sánchez-Lavega, A., 2008. Distribution of the O2 infrared nightglow observed with VIRTIS on board Venus express. Geophys. Res. Lett. 35. https://doi.org/10.1029/2007GL032021.

Gérard, J.-C., Soret, L., Saglam, A., Piccioni, G., Drossart, P., 2010. The distributions of the OH Meinel and O2(a1Δ–X3Σ) nightglow emissions in the Venus mesosphere based on VIRTIS observations. Adv. Space Res. 45, 1268–1275. https://doi.org/10.1016/j.asr.2010.01.022.

Gérard, J.-C., Soret, L., Piccioni, G., Drossart, P., 2014. Latitudinal structure of the Venus O2 infrared airglow: a signature of small-scale dynamical processes in the upper atmosphere. Icarus 236, 92–103. https://doi.org/10.1016/j.icarus.2014.03.028.

Gorinov, D.A., Khatuntsev, I.V., Zasova, L.V., Turin, A.V., Piccioni, G., 2018. Circulation of Venusian atmosphere at 90–110 km based on apparent motions of the O2 1.27 μm nightglow from VIRTIS-M (Venus express) data. Geophys. Res. Lett. 45, 2554–2562. https://doi.org/10.1002/2017GL076380.

Haus, R., Kappel, D., Tellmann, S., Arnold, G., Piccioni, G., Drossart, P., Häusler, B., 2016. Radiative energy balance of Venus based on improved models of the middle and lower atmosphere. Icarus 272, 178–205. https://doi.org/10.1016/j.icarus.2016.02.048.

Hoshino, N., Fujiwara, H., Takagi, M., Takahashi, Y., Kasaba, Y., 2012. Characteristics of planetary-scale waves simulated by a new venusian mesosphere and thermosphere general circulation model. Icarus 217, 818–830. https://doi.org/10.1016/j.icarus.2011.06.039. Advances in Venus Science.

Hueso, R., Sánchez-Lavega, A., Piccioni, G., Drossart, P., Gérard, J.C., Khatuntsev, I., Zasova, L., Migliorini, A., 2008. Morphology and dynamics of Venus oxygen airglow from Venus express/visible and infrared thermal imaging spectrometer observations. J. Geophys. Res. Planets 113. https://doi.org/10.1029/2008JE003081.

Judge, D.L., McMullin, D.R., Ogawa, H.S., Hovestadt, D., Klecker, B., Hilchenbach, M., Möbius, E., Canfield, L.R., Vest, R.E., Watts, R., Tarrio, C., Kühne, M., Wurz, P., 1998. First solar EUV irradiances obtained from SOHO by the CELIAS/SEM. In: Pap, J.M., Fröhlich, C., Ulrich, R.K. (Eds.), Solar Electromagnetic Radiation Study for Solar Cycle 22. Springer, Netherlands, Dordrecht, pp. 161–173. https://doi.org/10.1007/978-94-011-5000-2_12.

Khatuntsev, I.V., Patsaeva, M.V., Titov, D.V., Ignatiev, N.I., Turin, A.V., Fedorova, A.A., Markiewicz, W.J., 2017. Winds in the middle cloud deck from the near-IR imaging by the Venus monitoring camera onboard Venus express. J. Geophys. Res. (Planets) 122, 2312. https://doi.org/10.1002/2017JE005355.

Korablev, O., Bertaux, J.-L., Fedorova, A., Fonteyn, D., Stepanov, A., Kalinnikov, Y., Kiselev, A., Grigoriev, A., Jegoulev, V., Perrier, S., Dimarellis, E., Dubois, J.P., Reberac, A., Van Ransbeeck, E., Gondet, B., Montmessin, F., Rodin, A., 2006. SPICAM IR acousto-optic spectrometer experiment on Mars express. J. Geophys. Res. 111. https://doi.org/10.1029/2006JE002696. E09S03.

Korablev, O., Fedorova, A., Bertaux, J.-L., Stepanov, A.V., Kiselev, A., Kalinnikov, Yu.K., Titov, A.Yu., Montmessin, F., Dubois, J.P., Villard, E., Sarago, V., Belyaev, D., Reberac, A., Neefs, E., 2012. SPICAV IR acousto-optic spectrometer experiment on Venus express. Planet. Space Sci. 65, 38–57. https://doi.org/10.1016/j.pss.2012.01.002.

Kouyama, T., Imamura, T., Taguchi, M., Fukuhara, T., Sato, T.M., Yamazaki, A., Futaguchi, M., Murakami, S., Hashimoto, G.L., Ueno, M., Iwagami, N., Takagi, S., Takagi, M., Ogohara, K., Kashimura, H., Horinouchi, T., Sato, N., Yamada, M., Yamamoto, Y., Ohtsuki, S., Sugiyama, K., Ando, H., Takamura, M., Yamada, T., Satoh, T., Nakamura, M., 2017. Topographical and local time dependence of large stationary gravity waves observed at the cloud top of Venus. Geophys. Res. Lett. 44, 12,098-12,105. doi:https://doi.org/10.1002/2017GL075792.

Krasnopolsky, V.A., 2006. Chemical composition of Venus atmosphere and clouds: some unsolved problems. Planet. Space Sci. 54, 1352–1359. https://doi.org/10.1016/j.pss.2006.04.019. The Planet Venus and the Venus Express Mission.

Krasnopolsky, V.A., 2010. Venus night airglow: ground-based detection of OH, observations of O2 emissions, and photochemical model. Icarus 207, 17–27. https://doi.org/10.1016/j.icarus.2009.10.019.

Lellouch, E., Clancy, T., Crisp, D., Kliore, A.J., Titov, D., Bougher, S.W., 1997. Monitoring of mesospheric structure and dynamics. In: Venus II: Geology, Geophysics, Atmosphere, and Solar Wind Environment. University of Arizona Press, Tucson, pp. 295–324.

Markiewicz, W.J., Titov, D.V., Ignatiev, N., Keller, H.U., Crisp, D., Limaye, S.S., Jaumann, R., Moissl, R., Thomas, N., Esposito, L., Watanabe, S., Fiethe, B., Behnke, T., Szemerey, I., Michalik, H., Perplies, H., Wedemeier, M., Sebastian, I., Boogaerts, W., Hviid, S.F., Dierker, C., Osterloh, B., Böker, W., Koch, M., Michaelis, H., Belyaev, D., Dannenberg, A., Tschimmel, M., Russo, P., Roatsch, T., Matz, K.D., 2007. Venus monitoring camera for Venus express. Planet. Space Sci. 55 (12), 1701–1711. https://doi.org/10.1016/j.pss.2007.01.004.

Martinez, A., Lebonnois, S., Millour, E., Pierron, T., Moisan, E., Gilli, G., Lefèvre, F., 2023. Exploring the variability of the venusian thermosphere with the IPSL Venus GCM. Icarus 389, 115272. https://doi.org/10.1016/j.icarus.2022.115272.

Masunaga, K., Seki, K., Terada, N., Tsuchiya, F., Kimura, T., Yoshioka, K., Murakami, G., Yamazaki, A., Kagitani, M., Tao, C., Fedorov, A., Futaana, Y., Zhang, T.L., Shiota, D., Leblanc, F., Chaufray, J.-Y., Yoshikawa, I., 2015. Periodic variations of oxygen EUV dayglow in the upper atmosphere of Venus: Hisaki/EXCEED observations. J. Geophys. Res. Planets 120, 2037–2052. https://doi.org/10.1002/2015JE004849.

Masunaga, K., Seki, K., Terada, N., Tsuchiya, F., Kimura, T., Yoshioka, K., Murakami, G., Yamazaki, A., Tao, C., Leblanc, F., Yoshikawa, I., 2017. Dawn-dusk difference of periodic oxygen EUV dayglow variations at Venus observed by Hisaki. Icarus 292, 102–110. https://doi.org/10.1016/j.icarus.2016.12.027.

Miller, H.C., McCord, J.E., Choy, J., Hager, G.D., 2001. Measurement of the radiative lifetime of O2(a1Δg) using cavity ring down spectroscopy. J. Quant. Spectrosc. Radiat. Transf. 69, 305–325. https://doi.org/10.1016/S0022-4073(00)00086-8.

Mills, F.P., 1999. A spectroscopic search for molecular oxygen in the Venus middle atmosphere. J. Geophys. Res. Planets 104, 30757–30763. https://doi.org/10.1029/1999JE001085.

Mingalev, I.V., Rodin, A.V., Orlov, K.G., 2015. Numerical simulations of the global circulation of the atmosphere of Venus: effects of surface relief and solar radiation heating. Sol. Syst. Res. 49, 24–42. https://doi.org/10.1134/S0038094614060057.

Mishchenko, M.I., Travis, L.D., Lacis, A.A., 2002. Scattering, Absorption, and Emission of Light by Small Particles. Cambridge University Press.

Nara, Y., Imamura, T., Murakami, S., Kouyama, T., Ogohara, K., Yamada, M., Takagi, M., Kashimura, H., Sato, N., 2019. Formation of the Y feature at the Venusian cloud top by planetary-scale waves and the mean circulation: analysis of Venus express VMC images. J. Geophys. Res. Planets 124, 1143–1156. https://doi.org/10.1029/2018JE005779.

Nara, Y., Imamura, T., Masunaga, K., Lee, Y.J., Terada, N., Yoshioka, K., Yamazaki, A., Seki, K., Yoshikawa, I., Yamada, M., Watanabe, S., 2020. Vertical coupling between the cloud-level atmosphere and the thermosphere of Venus inferred from the simultaneous observations by Hisaki and Akatsuki. J. Geophys. Res. Planets 125. https://doi.org/10.1029/2019JE006192 e2019JE006192.

Navarro, T., Gilli, G., Schubert, G., Lebonnois, S., Lefèvre, F., Quirino, D., 2021. Venus' upper atmosphere revealed by a GCM: I. Structure and variability of the circulation. Icarus 366, 114400. https://doi.org/10.1016/j.icarus.2021.114400.

Ohtsuki, S., Iwagami, N., Sagawa, H., Kasaba, Y., Ueno, M., Imamura, T., 2005. Ground-based observation of the Venus 1.27-μm O2 airglow. Adv. Space Res. 36, 2038–2042. https://doi.org/10.1016/j.asr.2005.05.078. Planetary Atmospheres, Ionospheres, and Magnetospheres.

Ohtsuki, S., Iwagami, N., Sagawa, H., Ueno, M., Kasaba, Y., Imamura, T., Nishihara, E., 2008a. Imaging spectroscopy of the Venus 1.27-μm O2 airglow with ground-based telescopes. Adv. Space Res. 41, 1375–1380. https://doi.org/10.1016/j.asr.2007.10.014.

Ohtsuki, S., Iwagami, N., Sagawa, H., Ueno, M., Kasaba, Y., Imamura, T., Yanagisawa, K., Nishihara, E., 2008b. Distributions of the Venus 1.27-μm O2 airglow and rotational temperature. Planet. Space Sci. 56, 1391–1398. https://doi.org/10.1016/j.pss.2008.05.013. Ground-based and Venus Express Coordinated Campaign.

Palmer, K.F., Williams, D., 1975. Optical constants of sulfuric acid; application to the clouds of Venus? Appl. Opt. 14, 208–219. https://doi.org/10.1364/AO.14.000208.

Piccialli, A., Montmessin, F., Belyaev, D., Mahieux, A., Fedorova, A., Marcq, E., Bertaux, J.-L., Tellmann, S., Vandaele, A.C., Korablev, O., 2015. Thermal structure of Venus nightside upper atmosphere measured by stellar occultations with SPICAV/Venus express. Planet. Space Sci. 113–114, 321–335. https://doi.org/10.1016/j.pss.2014.12.009. SI:Exploration of Venus.

Piccioni, G., Zasova, L., Migliorini, A., Drossart, P., Shakun, A., García Muñoz, A., Mills, F.P., Cardesin-Moinelo, A., 2009. Near-IR oxygen nightglow observed by VIRTIS in the Venus upper atmosphere. J. Geophys. Res. Planets 114. https://doi.org/10.1029/2008JE003133.

Pollack, J.B., Dalton, J.B., Grinspoon, D., Wattson, R.B., Freedman, R., Crisp, D., Allen, D. A., Bezard, B., DeBergh, C., Giver, L.P., Ma, Q., Tipping, R., 1993. Near-infrared light from Venus' Nightside: a spectroscopic analysis. Icarus 103, 1–42. https://doi.org/10.1006/icar.1993.1055.

Richards, P.G., Fennelly, J.A., Torr, D.G., 1994. EUVAC: A solar EUV Flux Model for aeronomic calculations. J. Geophys. Res. Space Physics 99, 8981–8992. https://doi.org/10.1029/94JA00518.

Saunders, R.S., Spear, A.J., Allin, P.C., Austin, R.S., Berman, A.L., Chandlee, R.C., Clark, J., Decharon, A.V., De Jong, E.M., Griffith, D.G., Gunn, J.M., 1992. Magellan mission summary. J. Geophys. Re.: Planets 97, 13067–13090.

Seiff, A., Schofield, J.T., Kliore, A.J., Taylor, F.W., Limaye, S.S., Revercomb, H.E., Sromovsky, L.A., Kerzhanovich, V.V., Moroz, V.I., Marov, M.Ya., 1985. Models of the structure of the atmosphere of Venus from the surface to 100 kilometers altitude. Adv. Space Res. 5, 3–58. https://doi.org/10.1016/0273-1177(85)90197-8.

Shakun, A.V., Zasova, L.V., Piccioni, G., Drossart, P., Migliorini, A., 2010. Investigation of oxygen O2(a1Δg) emission on the nightside of Venus: nadir data of the VIRTIS-M experiment of the Venus express mission. Cosm. Res. 48, 232–239. https://doi.org/10.1134/S0010952510030044.

Shakun, A.V., Zasova, L.V., Gorinov, D.A., Khatuntsev, I.V., Ignatiev, N.I., Patsaeva, M. V., Turin, A.V., 2023. O2 (a1Δg) airglow at 1.27 μM and upper mesosphere dynamics on the night side of Venus. Sol. Syst. Res. 57, 200–213. https://doi.org/10.1134/S0038094623030085.

Solomon, S.C., Woods, T.N., Didkovsky, L.V., Emmert, J.T., Qian, L., 2010. Anomalously low solar extreme-ultraviolet irradiance and thermospheric density during solar minimum. Geophys. Res. Lett. 37. https://doi.org/10.1029/2010GL044468.

Soret, L., Gérard, J.-C., 2015. Is the O2(a1Δg) Venus nightglow emission controlled by solar activity? Icarus 262, 170–172. https://doi.org/10.1016/j.icarus.2015.08.030.

Soret, L., Gérard, J.-C., Montmessin, F., Piccioni, G., Drossart, P., Bertaux, J.-L., 2012. Atomic oxygen on the Venus nightside: global distribution deduced from airglow mapping. Icarus 217, 849–855. https://doi.org/10.1016/j.icarus.2011.03.034. Advances in Venus Science.

Soret, L., Gérard, J.-C., Piccioni, G., Drossart, P., 2014. Time variations of O2(a1Δ) nightglow spots on the Venus nightside and dynamics of the upper mesosphere. Icarus 237, 306–314. https://doi.org/10.1016/j.icarus.2014.03.034.

Sun, K., Gordon, I.E., Sioris, C.E., Liu, X., Chance, K., Wofsy, S.C., 2018. Reevaluating the use of O2 a1Δg band in spaceborne remote sensing of greenhouse gases. Geophys. Res. Lett. 45, 5779–5787. https://doi.org/10.1029/2018GL077823.

Takagi, M., Ando, H., Sugimoto, N., Matsuda, Y., 2022. A GCM study on the 4-day and 5-day waves in the Venus atmosphere. J. Geophys. Res. Planets 127. https://doi.org/10.1029/2021JE007164 e2021JE007164.

Tashkun, S.A., Perevalov, V.I., Teffo, J.-L., Bykov, A.D., Lavrentieva, N.N., 2003. CDSD-1000, the high-temperature carbon dioxide spectroscopic databank. J. Quant. Spectrosc. Radiat. Transf. 82, 165–196. https://doi.org/10.1016/S0022-4073(03)00152-3. The HITRAN Molecular Spectroscopic Database: Edition of 2000 Including Updates of 2001.

Taylor, F.W., Crisp, D., Bézard, B., 1997. Near-infrared sounding of the lower atmosphere of Venus. In: Bougher, S.W., Hunten, D.M., Phillips, R.J. (Eds.), Venus II: Geology, Geophysics, Atmosphere, and Solar Wind Environment. The University of Arizona Press, Tucson, pp. 325–351.

Tobiska, W.K., Woods, T., Eparvier, F., Viereck, R., Floyd, L., Bouwer, D., Rottman, G., White, O.R., 2000. The SOLAR2000 empirical SOLAR irradiance model and forecast tool. J. Atmospheric Sol.-Terr. Phys. 62, 1233–1250. https://doi.org/10.1016/S1364-6826(00)00070-5. Space Weather Week.

Woods, T.N., Harder, J.W., Kopp, G., Snow, M., 2022. Solar-cycle variability results from the solar radiation and climate experiment (SORCE) mission. Sol. Phys. 297, 43. https://doi.org/10.1007/s11207-022-01980-z.